Chemical Abundances in the Ultra-faint Dwarf Galaxies Grus I and Triangulum II: Neutron-capture Elements as a Defining Feature of the Faintest Dwarfs

The Astrophysical Journal, 870:83 (18pp), 2019 January 10 https://doi.org/10.3847/1538-4357/aaf3bb

Chemical Abundances in the Ultra-faint Dwarf Galaxies Grus I and Triangulum II: Neutron-capture Elements as a Defining Feature of the Faintest Dwarfs*

Alexander P. Ji[1,4], Joshua D. Simon[1], Anna Frebel[2], Kim A. Venn[3], and Terese T. Hansen[1]
[1] The Observatories of the Carnegie Institution for Science, 813 Santa Barbara St., Pasadena, CA 91101, USA; aji@carnegiescience.edu
[2] Department of Physics and Kavli Institute for Astrophysics and Space Research, Massachusetts Institute of Technology, Cambridge, MA 02139, USA
[3] Department of Physics and Astronomy, University of Victoria, Victoria, BC V8W 3P2, Canada
Received 2018 September 6; revised 2018 November 14; accepted 2018 November 22; published 2019 January 11

Abstract

We present high-resolution spectroscopy of four stars in two candidate ultra-faint dwarf galaxies (UFDs), Grus I (Gru I) and Triangulum II (Tri II). Neither object currently has a clearly determined velocity dispersion, placing them in an ambiguous region of parameter space between dwarf galaxies and globular clusters (GCs). No significant metallicity difference is found for the two Gru I stars, but both stars are deficient in neutron-capture elements. We verify previous results that Tri II displays significant spreads in metallicity and [α/Fe]. Neutron-capture elements are not detected in our Tri II data, but we place upper limits at the lower envelope of Galactic halo stars, consistent with previous very low detections. Stars with similarly low neutron-capture element abundances are common in UFDs but rare in other environments. This signature of low neutron-capture element abundances traces chemical enrichment in the least massive star-forming dark matter halos and further shows that the dominant sources of neutron-capture elements in metal-poor stars are rare. In contrast, all known GCs have similar ratios of neutron-capture elements to those of halo stars, suggesting that GCs do not form at the centers of their own dark matter halos. The low neutron-capture element abundances may be the strongest evidence that Gru I and Tri II are (or once were) galaxies rather than GCs, and we expect future observations of these systems to robustly find nonzero velocity dispersions or signs of tidal disruption. However, the nucleosynthetic origin of this low neutron-capture element floor remains unknown.

Key words: galaxies: dwarf – galaxies: individual (Gru I, Tri II) – Local Group – nuclear reactions, nucleosynthesis, abundances – stars: abundances

Supporting material: machine-readable table

1. Introduction

Ultra-faint dwarf galaxies (UFDs) are the least luminous galaxies known. They have only been discovered relatively recently, after the advent of deep, wide-area photometric surveys like the Sloan Digital Sky Survey, Pan-STARRS, and the Dark Energy Survey, which found several low surface brightness satellites of the Milky Way (e.g., Willman et al. 2005; Belokurov et al. 2007; Bechtol et al. 2015; Koposov et al. 2015a; Laevens et al. 2015). Though at first it was unclear whether such objects were dwarf galaxies or globular clusters (GCs; Willman et al. 2005), subsequent spectroscopic follow-up found that most of them displayed velocity dispersions implying mass-to-light ratios >100 and large metallicity spreads (e.g., Simon & Geha 2007). These properties contrast with GCs, which display no evidence for dark matter or large metallicity spreads (Willman & Strader 2012).

UFDs are now understood to be the natural result of galaxy formation in small dark matter halos in standard ΛCDM cosmology. Theoretically, these galaxies begin forming at $z \sim 10$ in small ($\sim 10^8\,M_\odot$) dark matter halos (Bromm & Yoshida 2011). Supernova (SN) feedback is especially effective in these small galaxies (e.g., Bland-Hawthorn et al. 2015), so they form stars inefficiently for 1–2 Gyr before their star formation is quenched by reionization (Bullock et al. 2000; Benson et al. 2002). All observed properties of UFDs are also consistent with this picture. Color–magnitude diagrams (CMDs) show that they contain uniformly old stellar populations (Brown et al. 2014; Weisz et al. 2014). Spectroscopy shows that their stars have low metallicities that extend the mass–metallicity relation all the way to $M_\star \sim 1000\,M_\odot$ (Kirby et al. 2008, 2013b). At such tiny stellar masses, the chemical abundances of individual UFDs will not even sample a full initial mass function's worth of SNe (e.g., Koch et al. 2008; Simon et al. 2010; Lee et al. 2013), let alone rarer nucleosynthesis events like neutron star mergers (Ji et al. 2016a).

Given the likely association between UFDs and small-scale dark matter substructure, it is extremely important to distinguish between UFDs and GCs. Currently, the largest telescopes can perform spectroscopy to establish velocity and metallicity dispersions from a reasonable number of stars in the closest and/or most luminous UFDs (e.g., Simon & Geha 2007). However, many of the most recently discovered UFDs are very faint and/or far away. In such cases, only a handful of stars are accessible for follow-up spectroscopy, so it is difficult to clearly establish a velocity or metallicity dispersion for these galaxy candidates (e.g., Koch et al. 2009; Kirby et al. 2015a, 2015b; Koposov et al. 2015b; Martin et al. 2016a, 2016b). Exacerbating this concern is the presence of unresolved binary stars, which can inflate velocity dispersions and can therefore lead to premature UFD classifications (McConnachie & Côté 2010; Ji et al. 2016d; Kirby et al. 2017). As a result, many UFD candidates still do not have clear velocity and/or metallicity dispersions (Kirby et al. 2015a, 2017; Martin et al. 2016a, 2016b; Walker et al. 2016; Simon et al. 2017).

* This paper includes data gathered with the 6.5 m Magellan Telescopes located at Las Campanas Observatory, Chile.
[4] Hubble Fellow.

For some UFDs, an alternative is to examine the detailed chemical abundances of the brightest stars. The first high-resolution spectroscopic abundances of stars in UFDs revealed that most elemental abundances in UFDs follow the average trends defined by metal-poor Milky Way halo stars, with the obvious exception of neutron-capture elements (e.g., Sr, Ba, Eu) that were extremely *low* (Koch et al. 2008, 2013; Frebel et al. 2010b, 2014; Simon et al. 2010). This view was recently revised by the discovery that some UFDs (Reticulum II and Tucana III) have extremely high abundances of neutron-capture elements synthesized in the *r*-process (Ji et al. 2016a; Roederer et al. 2016; Hansen et al. 2017). In stark contrast, neutron-capture elements in GCs closely follow the abundance trends of the Milky Way halo (e.g., Gratton et al. 2004, 2012; Pritzl et al. 2005), including the GCs that display some internal neutron-capture abundance scatter (Roederer 2011). Extreme neutron-capture element abundances have thus been suggested to be a distinguishing factor between UFDs and GCs (Frebel & Norris 2015).

Here we study the detailed chemical abundances of the dwarf galaxy candidates Grus I (Gru I) and Triangulum II (Tri II). Gru I was discovered in Dark Energy Survey data by Koposov et al. (2015a). Walker et al. (2016) identified seven likely members of this galaxy but did not resolve a metallicity or velocity dispersion. Tri II was discovered by Laevens et al. (2015) in Pan-STARRS. As one of the closest but also least luminous galaxy candidates ($d_{\odot} = 28.4$ kpc, $M_V = -1.2$; Carlin et al. 2017), Tri II has already been the subject of numerous spectroscopic studies (Kirby et al. 2015a, 2017; Martin et al. 2016b; Venn et al. 2017). We report the first detailed chemical abundances of two stars in Gru I and a reanalysis of two stars in Tri II with additional data. We describe our observations and abundance analysis in Sections 2 and 3. Section 4 details the results for individual elements. We consider the classification of Gru I and Tri II in Section 5, with an extended discussion of the origin and interpretation of neutron-capture elements in UFDs, larger dSph satellites, and GCs. We conclude in Section 6.

2. Observations and Data Reduction

Our program stars were observed from two telescopes with two different echelle spectrographs. Details of the observations can be found in Table 1. Selected spectral regions of these four stars are shown in Figure 1.

The Gru I stars were selected as the two brightest probable members of Gru I from Walker et al. (2016). We observed these stars with the Magellan Inamori Kyocera Echelle (MIKE) spectrograph (Bernstein et al. 2003) on the Magellan-Clay telescope in 2017 August with the 1.″0 slit, providing resolution $R \sim 28{,}000$ from ∼3900 to 5000 Å on the blue arm and $R \sim 22{,}000$ from ∼5000 to 9000 Å on the red arm. Individual exposures were 50–55 minutes long. The data were reduced with CarPy (Kelson 2003). Heliocentric corrections were determined with `rvcor` in IRAF.[5]

The two stars in Tri II were observed with the Gemini Remote Access to CFHT ESPaDOnS Spectrograph (GRACES; Donati 2003; Chene et al. 2014).[6] These stars were selected as the brightest probable members of Tri II from Kirby et al. (2015a) and Martin et al. (2016b). We combined data from two programs[7] that both used the two-fiber object+sky GRACES mode providing $R \sim 40{,}000$ from ∼5000 to 10000 Å. The GRACES throughput for these faint stars was worse than predicted by the integration time calculator, especially at wavelengths <6000 Å where the signal-to-noise ratio (S/N) was less than half that expected. The data were reduced with the OPERA pipeline for ESPaDOnS that was adapted for GRACES (Martioli et al. 2012). This pipeline automatically includes a heliocentric velocity correction.

We used IRAF and SMH (Casey 2014) to co-add, normalize, stitch orders, and Doppler-correct the reduced spectra. We estimated the S/N per pixel on co-added spectra by running a median absolute deviation filter across the normalized spectra in a ≈5 Å window. The S/N at the order center closest to rest wavelengths of 4500, 5300, and 6500 Å is given in Table 1. Radial velocities were determined by cross-correlating the Mg *b* triplet against a MIKE spectrum of HD 122563. Venn et al. (2017) found one of the stars in Tri II (TriII-46) to be a binary, so we Doppler-shifted spectra from each visit to rest frame before co-adding. The implications of this binary star were previously considered in Venn et al. (2017) and Kirby et al. (2017). Our added velocity measurement does not affect their conclusions.

Other than TriII-46, the velocities are consistent with constant heliocentric velocity in our data and with previous velocity measurements (Kirby et al. 2015a, 2017; Martin et al. 2016b; Walker et al. 2016; Venn et al. 2017). Velocity precision was estimated using the co-added spectra by cross-correlating all orders from 5000 to 6500 Å for MIKE and from 4500 to 6500 Å for GRACES against HD 122563. We excluded orders where the velocity was not within 10 km s^{-1} of the Mg *b* velocity and then took the standard deviation of the remaining order velocities. This value was added in quadrature to the combined statistical velocity uncertainty to obtain the velocity uncertainties listed in Table 1. The most discrepant velocity other than TriII-46 is for GruI-032, which is ≈1 km s^{-1} away from the measurement in Walker et al. (2016; -138.4 ± 0.4 km s^{-1}), but not large enough that we would consider this a clear binary candidate. Note that the two Gru I stars differ by ≈4 km s^{-1}, which could be consistent with a significant velocity dispersion.

3. Abundance Analysis

We analyzed all four stars using the 2011 version of the 1D LTE radiative transfer code MOOG (Sneden 1973; Sobeck et al. 2011) with the Castelli & Kurucz (2004; ATLAS) model atmospheres. We measured equivalent widths and ran MOOG with SMH (Casey 2014). The abundance of most elements was determined from equivalent widths. We used spectral synthesis to account for blends, molecules, and hyperfine structure for the species CH, Sc, Mn, Sr, Ba, and Eu. Atomic data references can be found in Table 3 of Roederer et al. (2010). Measurements and uncertainties of individual features are in Table 2. Stellar parameters and uncertainties for this work and previous measurements are in Table 3. Final abundances and uncertainties are in Table 4. Detailed abundance uncertainties due to stellar parameter variations are in Table 5.

[5] IRAF is distributed by the National Optical Astronomy Observatory, which is operated by the Association of Universities for Research in Astronomy (AURA) under a cooperative agreement with the National Science Foundation.

[6] See http://www.gemini.edu/sciops/instruments/visiting/graces for more details.

[7] GN-2015B-DD-2 (PI Venn) and GN-2016B-Q-44 (PI Ji).

Table 1
Observing Details

Star	α (J2000)	δ (J2000)	V (mag)	Observation Date	t_{exp} (minutes)	v_{hel} (km s^{-1})	S/N (4500 Å)	S/N (5300 Å)	S/N (6500 Å)	Instrument
GruI-032	22 56 58.1	−50 13 57.9	18.1	2017 Aug 16, 25	165	−139.8 ± 0.7	22	25	60	MIKE 1.″0 slit
GruI-038	22 56 29.9	−50 04 33.3	18.7	2017 Aug 15, 16, 25	430	−143.9 ± 0.4	20	22	55	MIKE 1.″0 slit
TriII-40	02 13 16.5	+36 10 45.9	17.3	2015 Dec 15	60	−381.5 ± 1.3	5	15	35	GRACES 2-fiber
				2016 Sep 8	80	−381.5				GRACES 2-fiber
TriII-46	02 13 21.5	+36 09 57.6	18.8	2015 Dec 16, 17	160	−396.5 ± 3.2	1	7	17	GRACES 2-fiber
				2016 Sep 7	120	−381.5 ± 5.0				GRACES 2-fiber

Note. S/N values are per pixel. S/N values for Tri II stars were determined after co-adding. Velocity precision is computed with co-added spectra except for TriII-46, where each visit is measured separately because of the binary orbital motion.

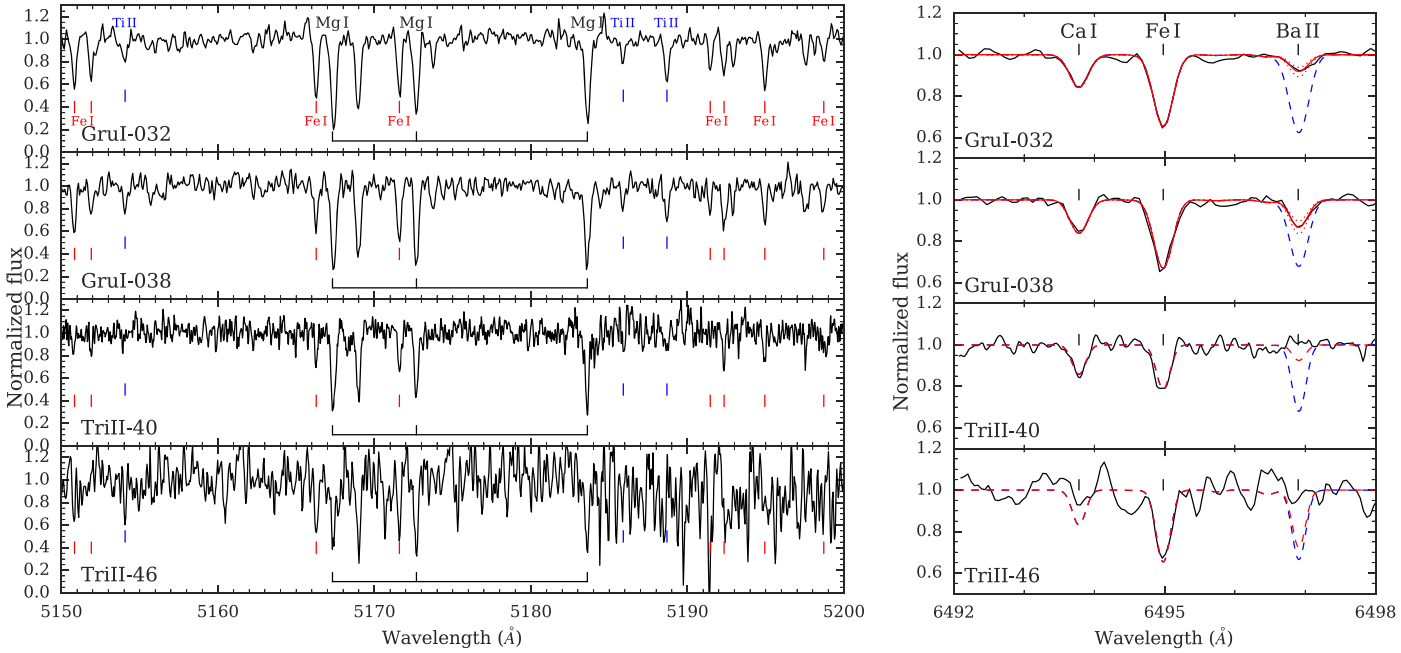

Figure 1. Left panels: spectra of the target stars around the Mg *b* triplet. Mg *b*, Ti II, and Fe I lines are labeled in black, blue, and red, respectively. Notice the large drop in S/N in TriII-46 at the red end due to reaching the order edge. Right panels: our four stars near the Ba line at 6497 Å. For Gru I stars, the solid red curve indicates our best-fit synthesis, while the dotted red curves indicate ±0.15 dex. For Tri II stars, the dashed red curves indicate upper limits. In all panels, the dashed blue line indicates [Ba/Fe] = 0 for comparison.

Table 2
Line Measurements

El.	λ (Å)	χ (eV)	log *gf* (dex)	EW	σ(EW)	log ϵ	σ(log ϵ)	EW	σ(EW)	log ϵ	σ(log ϵ)
				GruI-032				TriII-40			
CH	4313.00	⋯	⋯	syn	⋯	5.45	0.20	⋯	⋯	⋯	⋯
CH	4323.00	⋯	⋯	syn	⋯	5.25	0.30	⋯	⋯	⋯	⋯
Na I	5889.95	0.00	0.11	210.7	29.2	3.59	0.37	104.9	16.7	2.49	0.25
Na I	5895.92	0.00	−0.19	175.4	25.5	3.43	0.36	83.9	14.6	2.51	0.20

(This table is available in its entirety in machine-readable form.)

3.1. Standard Analysis for Brighter Stars

For three of our stars (GruI-032, GruI-038, and TriII-40), our spectra are of sufficient quality for a standard equivalent width analysis. We first fit Gaussian profiles to the line list in Roederer et al. (2010). We applied the formula from Battaglia et al. (2008) to determine equivalent width uncertainties. The S/N per pixel was calculated with median absolute deviation in a running 5 Å window. Varying the window size affected the S/N estimates by only 2%–3%, but we conservatively add an additional 10% uncertainty to each equivalent width. Using this estimate, we rejected most lines with equivalent width uncertainties larger than 30%. The exceptions were lines of Al, Si, Cr, Co, and Zn that otherwise would have had all lines of that element rejected and some clean lines near regions of large true variation (e.g., near CH bands), where the S/N was clearly underestimated. We propagate these to a 1σ abundance uncertainty for each line (Table 2). Synthesis uncertainties are calculated by varying abundances until the entire synthesized profile encompasses the spectrum noise around the feature, corresponding to 1σ uncertainties.

We derived the effective temperature, surface gravity, and microturbulence ($T_{\rm eff}$, $\log g$, ν_t) with excitation, ionization, and line strength balance of Fe lines. We then applied the $T_{\rm eff}$ correction from Frebel et al. (2013) and redetermined $\log g$ and ν_t. Statistical uncertainties for $T_{\rm eff}$ and ν_t correspond to the 1σ error on the fitted slopes of abundance with respect to excitation potential and reduced equivalent width, respectively. The statistical uncertainty for $\log g$ was derived by varying the parameter to match the combined standard error of the Fe I and Fe II abundances. We then further adopt systematic uncertainties of 150 K for $T_{\rm eff}$ from scatter in the Frebel et al. (2013) calibration, 0.3 dex for $\log g$, and 0.3 km s^{-1} for ν_t to reflect this systematic temperature uncertainty. We use the standard deviation of Fe I lines as the statistical uncertainty in the stellar atmosphere's model metallicity. We add the statistical and systematic uncertainties in quadrature to obtain the stellar parameter uncertainties in Table 3. These three stars are all α-enhanced, so we used the [α/Fe] = +0.4 Castelli & Kurucz (2004) model atmospheres.

3.2. Analysis of TriII-46

The data for star TriII-46 have very low S/N (Table 1) and thus require special care. We rebin the spectra by a factor of 2 to improve the S/N. This allowed us to measure equivalent

Table 3
Stellar Parameters

Star	References	$T_{\rm eff}$	σ	$\log g$	σ	ν_t[a]	σ	[Fe/H]	σ
GruI-032	TW	4495	155	0.85	0.37	2.60	0.32	−2.57	0.19
GruI-032	W16[b]	4270	69	0.72	0.22	2.0	⋯	−2.69	0.10
GruI-038	TW	4660	158	1.45	0.39	2.40	0.32	−2.50	0.24
GruI-038	W16[b]	4532	100	0.87	0.31	2.0	⋯	−2.42	0.15
TriII-40	TW	4720	175	1.35	0.42	2.48	0.34	−2.95	0.21
TriII-40	V17	4800	50	1.80	0.06	2.7	0.2	−2.87	0.19
TriII-40	K17[c]	4816	⋯	1.64	⋯	2.51	⋯	−2.92	0.21
TriII-40	K17[d]	4917	⋯	1.89	⋯	1.70	⋯	−2.78	0.11
TriII-46	TW	5150	200	2.7	0.5	2.00	0.5	−1.96	0.28
TriII-46	V17	5050	50	2.60	0.06	2.5	⋯	−2.5	0.2
TriII-46	K17[d]	5282	⋯	2.74	⋯	1.50	⋯	−1.91	0.11
TriII-46	Spec[e]	5260	240	2.7	0.6	2.5	0.5	−2.01	0.26

Notes.
[a] ν_t for W16 is always 2 km s^{-1} (Lee et al. 2008). ν_t for DEIMOS data in K17 according to the equation $\nu_t = 2.13 - 0.23 \log g$ (Kirby et al. 2009).
[b] [Fe/H] for W16 stars have a 0.32 dex offset removed; see text.
[c] HIRES data.
[d] DEIMOS data.
[e] Spectroscopic balances in this work using isochrones to determine $\log g$.
References. TW = this work; W16 = Walker et al. 2016; V17 = Venn et al. 2017; K17 = Kirby et al. 2017.

widths for lines at the center of echelle orders with wavelengths >5000 Å. After keeping only lines with equivalent width uncertainty less than 30%, we have 18 Fe I lines and only one Fe II line.

For this small number of lines, spectroscopic determination of stellar parameters is subject to many degeneracies based on line selection. Still, we examine here what parameters would be derived with the information from Fe lines. If we apply the same procedure as for the other three stars (i.e., excitation, ionization, and line strength balance with the Frebel et al. 2013 correction but using only these 19 lines), we obtain $T_{\rm eff} = 5260$ K, $\log g = 2.1$ dex, $\nu_t = 2.60$ km s^{-1}, and [Fe/H] = −2.01. However, the ionization equilibrium is set by a single Fe II line with equivalent width 164 ± 50 mÅ, so this is extremely unreliable. Ignoring the Fe II line and using an [Fe/H] = −2 Yonsei−Yale isochrone to set $\log g$ as a function of $T_{\rm eff}$ (Kim et al. 2002), we obtain $T_{\rm eff} = 5260$ K, $\log g = 2.7$ dex, $\nu_t = 2.50$ km s^{-1}, and [Fe/H] = −2.01. The statistical errors are large: 240 K, 0.6 dex, 0.5 km s^{-1}, and 0.3 dex, respectively.

We summarize this and other derived stellar parameters for this star in Table 3. For comparison, Venn et al. (2017) derived $T_{\rm eff} = 5050$ K, $\log g = 2.6$ dex, and $\nu_t = 2.5$ km s^{-1} for TriII-46 using photometry, distance, and a modified scaling relation for ν_t. An updated distance modulus (Carlin et al. 2017) would slightly increase $\log g$ to 2.7 dex. Kirby et al. (2017) derived $T_{\rm eff} = 5282$ K, $\log g = 2.74$ dex, and $\nu_t = 1.5$ km s^{-1} using photometry and distance to set $\log g$ and ν_t but allowing $T_{\rm eff}$ to vary to fit their spectrum. Our stellar parameters are somewhat in between their values, preferring the higher temperature from Kirby et al. (2017) but with the higher microturbulence from Venn et al. (2017). Our data for this star are insufficient to make any further refinements, so we decided to adopt intermediate values with large uncertainties that encompass other stellar parameter determinations: $T_{\rm eff} = 5150 \pm 200$ K, $\log g = 2.7 \pm 0.5$ dex, and $\nu_t = 2.0 \pm 0.5$ km s^{-1}. Regardless of the stellar parameters, this star is not α-enhanced, so we use the Castelli & Kurucz (2004) model atmospheres with $[\alpha/{\rm Fe}] = 0$. We propagate these uncertainties through to the final abundance uncertainties.

3.3. Final Abundances and Uncertainties

Table 4 contains the final abundance results for our stars. For each element, N is the number of lines measured. $\log \epsilon(X)$ is the average abundance of those lines weighted by the abundance uncertainty. Letting $\log \epsilon_i$ and σ_i be the abundance and uncertainty of line i, we define $w_i = 1/\sigma_i^2$ and $\log \epsilon(X) = \sum_i (w_i \log \epsilon_i)/\sum_i w_i$. σ is the standard deviation of those lines. $\sigma_{\rm w}$ is the standard error from propagating individual line uncertainties, i.e., $1/\sigma_{\rm w}^2 = \sum_i w_i$ (McWilliam et al. 1995). [X/H] is the abundance relative to solar abundances from Asplund et al. (2009). [X/Fe] is calculated using either [Fe I/H] or [Fe II/H], depending on whether X is neutral or ionized, except for TriII-46, where all [X/Fe] are calculated relative to [Fe I/H] because of an unreliable Fe II abundance. $\sigma_{\rm [X/H]}$ is the quadrature sum of $\sigma/\sqrt{N}$, $\sigma_{\rm w}$, and abundance uncertainties due to 1σ stellar parameter variations. Detailed abundance variations from changing each stellar parameter are given in Table 5. $\sigma_{\rm [X/Fe]}$ is similar to $\sigma_{\rm [X/H]}$, but when calculating the stellar parameter uncertainties, we include variations in Fe. We use the difference in Fe I abundance for neutral species and the difference in Fe II abundance for ionized species to calculate this error. The [X/Fe] error is usually smaller than the [X/H] error, since abundance differences from changing $T_{\rm eff}$ and $\log g$ usually (but not always) affect X and Fe in the same direction when using the same ionization state. Since most of our elements have very few lines, we adopt the standard deviation of the Fe I lines as the minimum σ when calculating $\sigma_{\rm [X/H]}$ and $\sigma_{\rm [X/Fe]}$.

Upper limits were derived by spectrum synthesis. Using several features of each element (Table 2), we found the best-fit synthesis to the observed spectrum to determine a reference χ^2 and smoothing for the synthetic spectrum. The minimum smoothing was calculated using FWHM = λ/R, where λ is the line wavelength. Holding the continuum, smoothing, and radial

Table 4
Abundances

Species	N	$\log \epsilon(X)$	σ	σ_w	[X/H]	$\sigma_{[X/H]}$	[X/Fe]	$\sigma_{[X/Fe]}$
				GruI-032				
CH	2	5.39	0.14	0.17	−3.04	0.40	−0.49	0.29
Na I	2	3.51	0.11	0.26	−2.73	0.50	−0.18	0.32
Mg I	5	5.45	0.12	0.13	−2.15	0.35	0.40	0.17
Al I	1	2.97	⋯	1.18	−3.48	1.27	−0.93	1.21
Si I	1	5.38	⋯	0.66	−2.13	0.75	0.42	0.70
K I	2	3.09	0.03	0.13	−1.94	0.31	0.61	0.20
Ca I	13	3.98	0.19	0.05	−2.36	0.20	0.20	0.13
Sc II	5	0.62	0.31	0.21	−2.53	0.32	−0.01	0.33
Ti I	11	2.53	0.22	0.07	−2.42	0.38	0.13	0.15
Ti II	26	2.65	0.19	0.05	−2.30	0.19	0.21	0.16
Cr I	9	2.91	0.17	0.07	−2.73	0.33	−0.18	0.12
Mn I	7	2.48	0.30	0.12	−2.95	0.38	−0.40	0.19
Fe I	112	4.95	0.19	0.02	−2.55	0.30	0.00	⋯
Fe II	10	4.98	0.25	0.09	−2.52	0.23	0.00	⋯
Co I	3	2.76	0.11	0.40	−2.23	0.61	0.32	0.45
Ni I	7	3.91	0.18	0.06	−2.31	0.29	0.24	0.11
Zn I	1	1.95	⋯	0.18	−2.61	0.28	−0.06	0.40
Sr II	2	−1.65	0.28	0.35	−4.52	0.45	−2.00	0.45
Ba II	4	−1.92	0.33	0.07	−4.10	0.25	−1.58	0.30
Eu II	1	<−1.68	⋯	⋯	<−2.20	⋯	<+0.32	⋯
				GruI-038				
CH	2	5.60	0.03	0.19	−2.83	0.45	−0.34	0.34
Na I	2	3.48	0.06	0.26	−2.76	0.48	−0.27	0.32
Mg I	5	5.34	0.19	0.12	−2.26	0.34	0.23	0.19
Al I	1	3.08	⋯	1.42	−3.37	1.49	−0.88	1.44
Si I	1	5.56	⋯	0.58	−1.95	0.69	0.54	0.63
K I	2	3.24	0.06	0.14	−1.79	0.34	0.71	0.23
Ca I	11	4.03	0.26	0.06	−2.31	0.21	0.19	0.16
Sc II	10	0.90	0.16	0.10	−2.25	0.25	0.21	0.26
Ti I	8	2.47	0.20	0.09	−2.48	0.33	0.02	0.14
Ti II	37	2.78	0.23	0.05	−2.17	0.22	0.29	0.17
Cr I	8	2.85	0.16	0.09	−2.79	0.35	−0.30	0.13
Mn I	7	2.49	0.26	0.10	−2.94	0.37	−0.45	0.17
Fe I	107	5.01	0.24	0.02	−2.49	0.31	0.00	⋯
Fe II	7	5.04	0.26	0.11	−2.46	0.25	0.00	⋯
Co I	1	2.86	⋯	0.74	−2.13	0.90	0.36	0.79
Ni I	5	3.98	0.10	0.07	−2.24	0.28	0.25	0.15
Sr II	2	−1.65	0.14	0.35	−4.52	0.44	−2.06	0.44
Ba II	4	−1.23	0.14	0.10	−3.41	0.25	−0.94	0.25
Eu II	1	<−1.20	⋯	⋯	<−1.72	⋯	<+0.74	⋯
				TriII-40				
Na I	2	2.50	0.01	0.16	−3.74	0.33	−0.79	0.22
Mg I	3	5.00	0.10	0.13	−2.60	0.32	0.35	0.20
K I	1	2.89	⋯	0.30	−2.14	0.36	0.81	0.31
Ca I	8	3.82	0.24	0.05	−2.52	0.20	0.43	0.15
Sc II	1	<0.98	⋯	⋯	<−2.17	⋯	<+0.65	⋯
Ti I	3	2.31	0.08	0.13	−2.64	0.32	0.31	0.19
Ti II	2	2.30	0.44	0.18	−2.65	0.40	0.17	0.40
Cr I	3	2.49	0.27	0.13	−3.15	0.35	−0.20	0.21
Mn I	1	<2.97	⋯	⋯	<−2.46	⋯	<+0.36	⋯
Fe I	60	4.55	0.21	0.02	−2.95	0.28	0.00	⋯
Fe II	5	4.68	0.33	0.09	−2.82	0.23	0.00	⋯
Ni I	3	3.84	0.19	0.09	−2.38	0.30	0.57	0.16
Ba II	1	<−1.89	⋯	⋯	<−4.07	⋯	<−1.25	⋯
Eu II	1	<−0.89	⋯	⋯	<−1.41	⋯	<+1.41	⋯
				TriII-46				
Na I	1	<5.27	⋯	⋯	<−0.97	⋯	<1.04	⋯
Mg I	2	5.12	0.02	0.42	−2.48	0.61	−0.47	0.53
K I	1	<3.79	⋯	⋯	<−1.24	⋯	<0.77	⋯

Table 4
(Continued)

Species	N	$\log\epsilon(X)$	σ	σ_w	[X/H]	$\sigma_{[X/H]}$	[X/Fe]	$\sigma_{[X/Fe]}$
Ca I	3	4.18	0.30	0.15	−2.16	0.33	−0.15	0.28
Sc II	1	<2.65	⋯	⋯	<−0.50	⋯	<1.51	⋯
Ti II	1	2.99	⋯	0.38	−1.96	0.53	0.05	0.98
Fe I	18	5.49	0.29	0.09	−2.01	0.36	0.00	⋯
Fe II	1	5.98	⋯	0.82	−1.52	0.92	0.49	⋯
Ni I	1	<5.36	⋯	⋯	<−0.86	⋯	<1.15	⋯
Ba II	1	<−0.06	⋯	⋯	<−2.24	⋯	<−0.23	⋯
Eu II	1	<0.50	⋯	⋯	<−0.02	⋯	<1.99	⋯

velocity fixed, we increased the abundance until $\Delta\chi^2 = 25$. This is formally a 5σ upper limit, though it does not include uncertain continuum placement.

3.4. Comparison to Literature Measurements

For the two Gru I stars, Walker et al. (2016) determined stellar parameters and metallicities from high-resolution M2FS spectra near the Mg b triplet using a large synthesized grid. The grid fixes $\nu_t = 2.0$ (Lee et al. 2008). Walker et al. (2016) increased all their [Fe/H] measurements by 0.32 dex, which is the offset they obtained from fitting twilight spectra of the Sun. It is not clear that the same offset should be applied for both dwarf stars (like the Sun) and giants. If we remove the offset, our stellar parameters and metallicities are in good agreement (see also Ji et al. 2016b).

Venn et al. (2017) analyzed both stars in Tri II, and we have combined their previous GRACES data with additional observations.[8] For TriII-40, we find good agreement for all stellar parameters except $\log g$. This is because we determined our $\log g$ spectroscopically, while Venn et al. (2017) did so photometrically using the distance to Tri II. Adjusting for the different $\log g$, our abundances for this star agree within 1σ. For TriII-46, Venn et al. (2017) fixed stellar parameters with photometry and used spectral synthesis to measure all abundances. We measured [Fe/H] $= -2.01 \pm 0.37$, while Venn et al. (2017) obtained [Fe/H] $= -2.5 \pm 0.2$. Our large abundance uncertainty means that these are only 1.2σ discrepant, but we might expect better agreement given that so many of the data overlap. Detailed investigation of the discrepancy shows that 0.3 dex of the difference is due to differences in stellar parameters (mostly $T_{\rm eff}$ and ν_t). The remaining 0.2 dex is attributable to systematic differences in continuum placement that are individually within 1σ uncertainties. Finally, we note that the stellar parameter uncertainties in Venn et al. (2017) reflect statistical photometric errors but could be larger owing to systematic uncertainties in photometric calibrations, filter conversions, and reddening maps.

Kirby et al. (2017) determined abundances of TriII-40 with a high-resolution, high-S/N Keck/HIRES spectrum. Our abundances agree within 0.15 dex, except for Cr, which is still within 1σ. Kirby et al. (2017) also analyzed the Mg, Ca, Ti, and Fe abundance of TriII-46 by matching a synthetic grid to an $R \sim 7000$ Keck/DEIMOS spectrum. They measured [Mg/Fe] $= +0.21 \pm 0.28$, [Ca/Fe] $= -0.39 \pm 0.15$, and [Ti/Fe] $= -0.79 \pm 0.76$. There are some significant discrepancies, especially for Mg. One possible reason for these differences is that we used stronger blue lines with lower excitation potentials for Mg and Ti, while the synthetic grid is driven by combining multiple higher-excitation potential lines that we could not individually measure in our spectrum. This explanation is supported by the fact that our Ca abundances agree better because they are derived from similar spectral features.

[8] Venn et al. (2017) labeled the stars as Star 40 and Star 46 instead of TriII-40 and TriII-46. We have retained the number but changed the label to TriII for clarity.

4. Abundance Results

In Gru I we measured the abundances of C, Na, Mg, Al, Si, K, Ca, Sc, Ti, Cr, Mn, Fe, Co, Ni, Sr, and Ba. In Tri II we were only able to measure Mg, K, Ca, Ti, Cr, Fe, Co, Ni, and Ba owing to a combination of lower S/N and the fact that the strongest features for other elements are found at $\lambda < 5000$ Å.

Figures 2, 3, and 4 show the abundances of our four stars compared to other UFDs and a literature sample of halo stars (Frebel 2010, and Roederer et al. 2014 for K). The UFDs are Bootes I (Feltzing et al. 2009; Norris et al. 2010; Gilmore et al. 2013; Ishigaki et al. 2014; Frebel et al. 2016), Bootes II (Ji et al. 2016a), CVn II (François et al. 2016), Coma Berenices (Frebel et al. 2010b), Hercules (Koch et al. 2008, 2013), Hor I (Nagasawa et al. 2018), Leo IV (Simon et al. 2010; François et al. 2016), Reticulum II (Ji et al. 2016c; Roederer et al. 2016), Segue 1 (Frebel et al. 2014), Segue 2 (Roederer & Kirby 2014), Tuc II (Ji et al. 2016b; Chiti et al. 2018), Tuc III (Hansen et al. 2017), and UMa II (Frebel et al. 2010b).

Overall, the two Gru I stars have the same [Fe/H] to within our abundance uncertainties, and all [X/Fe] ratios are very similar except for Ba. The metallicities of the Tri II stars differ by more than 2σ and display different abundance ratios. We now discuss each element in more detail.

4.1. Carbon

Spectral synthesis of the G-band features at 4313 and 4323 Å was used to measure carbon in the Gru I stars (using a list from B. Plez 2007, private communication). The oxygen abundance can affect molecular equilibrium, but since oxygen cannot be measured in these stars, we assume [O/Fe] $= 0.4$. Since they are red giant branch stars, some C has been converted to N. The corrections from Placco et al. (2014) were applied to estimate the natal abundance, which are [C/Fe] $= +0.21$ and $+0.57$ for GruI-032 and GruI-038, respectively. Varying $\log g$ by the uncertainty in Table 3 causes the correction to change by ± 0.1 dex. Both stars are carbon-normal ([C/Fe] < 0.7) even after this carbon correction. Note that the uncorrected carbon abundances are used in Figure 2 and Table 4.

We were unable to place any constraints on carbon in Tri II. The GRACES spectra are not usable below 4800 Å, so the G

Table 5
Stellar Parameter Abundance Uncertainties

	$\Delta T_{\rm eff}$ (K)		$\Delta \log g$ (cgs)		$\Delta\nu_t$ (km s^{-1})		Δ[Fe/H] (dex)		$\sigma_{\rm [X/H]}$	$\sigma_{\rm [X/Fe]}$
GruI-032	+155	−155	+0.37	−0.37	+0.32	−0.32	+0.19	−0.19		
[C/H]	+0.31	−0.22	−0.09	+0.11	−0.01	+0.01	+0.10	−0.09	0.34	0.19
[Na I/H]	+0.33	−0.36	−0.08	+0.08	−0.17	+0.17	−0.07	+0.06	0.41	0.14
[Mg I/H]	+0.27	−0.25	−0.11	+0.12	−0.09	+0.10	−0.04	+0.03	0.31	0.05
[Al I/H]	+0.32	−0.36	−0.12	+0.12	−0.19	+0.19	−0.06	+0.05	0.43	0.16
[Si I/H]	+0.24	−0.16	−0.06	+0.07	−0.13	+0.17	−0.04	+0.04	0.30	0.11
[K I/H]	+0.22	−0.21	−0.05	+0.06	−0.06	+0.07	−0.04	+0.03	0.24	0.06
[Ca I/H]	+0.17	−0.17	−0.06	+0.06	−0.05	+0.06	−0.04	+0.03	0.19	0.10
[Sc II/H]	+0.08	−0.05	+0.09	−0.08	−0.14	+0.16	+0.03	−0.02	0.20	0.17
[Ti I/H]	+0.28	−0.35	−0.07	+0.09	−0.05	+0.07	−0.05	+0.04	0.37	0.11
[Ti II/H]	+0.07	+0.02	+0.11	−0.11	−0.10	+0.12	+0.03	−0.02	0.18	0.09
[V I/H]	+0.27	−0.34	−0.06	+0.08	−0.03	+0.04	−0.04	+0.04	0.35	0.11
[Cr I/H]	+0.25	−0.30	−0.07	+0.08	−0.05	+0.07	−0.05	+0.04	0.32	0.06
[Cr II/H]	−0.02	+0.10	+0.13	−0.13	−0.02	+0.03	+0.02	−0.01	0.17	0.10
[Mn I/H]	+0.32	−0.32	−0.05	+0.07	−0.05	+0.08	−0.02	+0.02	0.34	0.09
[Fe I/H]	+0.26	−0.25	−0.06	+0.07	−0.09	+0.11	−0.05	+0.04	0.30	···
[Fe II/H]	+0.01	+0.11	+0.12	−0.12	−0.10	+0.12	+0.03	−0.02	0.20	···
[Co I/H]	+0.37	−0.33	−0.07	+0.09	−0.20	+0.24	−0.06	+0.06	0.45	0.17
[Ni I/H]	+0.25	−0.25	−0.04	+0.06	−0.05	+0.06	−0.04	+0.03	0.27	0.06
[Zn I/H]	+0.05	+0.00	+0.07	−0.06	−0.01	+0.01	+0.01	−0.01	0.09	0.30
[Sr II/H]	+0.01	−0.03	+0.07	−0.10	−0.15	+0.17	−0.01	−0.02	0.20	0.16
[Ba II/H]	+0.11	−0.08	+0.12	−0.10	−0.02	+0.03	+0.03	−0.02	0.17	0.21
GruI-038	+158	−158	+0.39	−0.39	+0.32	−0.32	+0.24	−0.24		
[C/H]	+0.31	−0.30	−0.15	+0.11	−0.01	+0.01	+0.09	−0.13	0.37	0.23
[Na I/H]	+0.21	−0.31	−0.08	+0.04	−0.17	+0.18	−0.06	+0.02	0.37	0.09
[Mg I/H]	+0.19	−0.26	−0.12	+0.08	−0.08	+0.08	−0.03	+0.00	0.30	0.09
[Al I/H]	+0.22	−0.30	−0.13	+0.09	−0.18	+0.18	−0.04	+0.02	0.38	0.12
[Si I/H]	+0.19	−0.22	−0.04	+0.02	−0.14	+0.17	−0.03	+0.02	0.28	0.08
[K I/H]	+0.17	−0.23	−0.04	+0.02	−0.08	+0.10	−0.03	+0.02	0.26	0.06
[Ca I/H]	+0.14	−0.18	−0.04	+0.02	−0.04	+0.05	−0.02	+0.01	0.19	0.12
[Sc II/H]	+0.11	−0.11	+0.06	−0.09	−0.16	+0.15	+0.01	−0.06	0.22	0.18
[Ti I/H]	+0.24	−0.30	−0.05	+0.03	−0.05	+0.07	−0.04	+0.02	0.31	0.05
[Ti II/H]	+0.03	−0.07	+0.12	−0.14	−0.10	+0.13	+0.03	−0.04	0.21	0.07
[Cr I/H]	+0.23	−0.30	−0.06	+0.03	−0.10	+0.11	−0.04	+0.02	0.33	0.02
[Mn I/H]	+0.24	−0.32	−0.08	+0.06	−0.07	+0.06	−0.02	+0.01	0.34	0.08
[Fe I/H]	+0.22	−0.28	−0.05	+0.03	−0.09	+0.12	−0.04	+0.02	0.31	···
[Fe II/H]	−0.03	+0.00	+0.14	−0.15	−0.09	+0.12	+0.03	−0.04	0.20	···
[Co I/H]	+0.26	−0.35	−0.07	+0.03	−0.22	+0.26	−0.07	+0.03	0.45	0.16
[Ni I/H]	+0.20	−0.24	−0.02	+0.02	−0.05	+0.07	−0.03	+0.01	0.25	0.07
[Sr II/H]	+0.04	−0.09	+0.05	−0.14	−0.11	+0.11	+0.00	−0.06	0.21	0.13
[Ba II/H]	+0.09	−0.10	+0.10	−0.12	−0.07	+0.09	+0.02	−0.04	0.19	0.13
TriII-40	+175	−175	+0.42	−0.42	+0.34	−0.34	+0.21	−0.21		
[Na I/H]	+0.20	−0.23	−0.05	+0.04	−0.06	+0.08	−0.01	+0.01	0.25	0.03
[Mg I/H]	+0.22	−0.22	−0.11	+0.11	−0.11	+0.10	−0.01	+0.01	0.27	0.09
[K I/H]	+0.15	−0.19	−0.04	+0.02	−0.03	+0.03	−0.01	+0.00	0.20	0.09
[Ca I/H]	+0.13	−0.16	−0.04	+0.03	−0.02	+0.03	−0.01	+0.00	0.17	0.11
[Ti I/H]	+0.21	−0.26	−0.06	+0.04	−0.03	+0.05	−0.01	+0.01	0.27	0.04
[Ti II/H]	+0.10	−0.07	+0.13	−0.11	−0.07	+0.10	+0.02	−0.01	0.19	0.08
[Cr I/H]	+0.22	−0.26	−0.06	+0.04	−0.06	+0.08	−0.01	+0.01	0.28	0.02
[Fe I/H]	+0.22	−0.26	−0.05	+0.04	−0.07	+0.08	−0.02	+0.01	0.28	···
[Fe II/H]	+0.03	−0.01	+0.14	−0.13	−0.06	+0.08	+0.01	−0.01	0.16	···
[Ni I/H]	+0.21	−0.25	−0.04	+0.04	−0.04	+0.05	−0.01	+0.01	0.26	0.03
TriII-46	+200	−200	+0.50	−0.50	+0.50	−0.50	+0.30	−0.30		
[Na I/H]	+0.18	−0.28	−0.13	+0.08	−0.20	+0.18	−0.02	−0.06	0.37	0.09
[Mg I/H]	+0.22	−0.29	−0.24	+0.22	−0.12	+0.08	+0.02	−0.05	0.40	0.23
[Ca I/H]	+0.14	−0.19	−0.05	+0.03	−0.10	+0.13	−0.00	−0.03	0.24	0.11
[Ti II/H]	+0.06	−0.07	+0.17	−0.17	−0.09	+0.13	+0.03	−0.04	0.23	0.24
[Fe I/H]	+0.21	−0.26	−0.06	+0.04	−0.16	+0.21	−0.01	−0.03	0.34	···

Table 5
(Continued)

	$\Delta T_{\rm eff}$ (K)		$\Delta \log g$ (cgs)		$\Delta\nu_t$ (km s^{-1})		Δ[Fe/H] (dex)		$\sigma_{\rm [X/H]}$	$\sigma_{\rm [X/Fe]}$
GruI-032	+155	−155	+0.37	−0.37	+0.32	−0.32	+0.19	−0.19		
[Fe II/H]	+0.04	−0.10	+0.03	−0.05	−0.28	+0.21	+0.03	−0.06	0.31	⋯

Note. $\sigma_{\rm [X/H]}$ is the quadrature sum of the maximum error for $\Delta T_{\rm eff}$, $\Delta \log g$, $\Delta\nu_t$, and Δ[Fe/H]. $\sigma_{\rm [X/Fe]}$ is the same sum but including the change in [Fe I/H] or [Fe II/H], depending on whether species X is neutral or ionized. Correlations between stellar parameters were not considered. Statistical uncertainties for both quantities are not included in this table, but they are in Table 4.

band cannot be measured. The CH lists from Masseron et al. (2014) and Kurucz (2011) do suggest that strong CH features should exist at 5893 and 8400 Å that were used to place a [C/Fe] upper limit by Venn et al. (2017), but we could not find these features in several carbon-enhanced metal-poor stars or atlas spectra of the Sun and Arcturus (Hinkle et al. 2003).[9] No other C features are available. Kirby et al. (2017) were able to measure [C/Fe] ~ -0.1 for TriII-40 from their HIRES spectrum, so this star is not carbon enhanced.

4.2. α-elements: Mg, Si, Ca, Ti

The abundances of these four α-elements are determined from equivalent widths. The magnesium abundance is determined from three to six lines, but always using two of the Mg *b* lines. Silicon can only be measured in the Gru I stars, using the line at 4102 Å that is in the wing of Hδ. The abundance uncertainty from only this single line is quite large, ≈0.6 dex. Neutral calcium is well determined by a large number of lines, and it should be considered the most reliable α-element. Titanium has several strong lines in both the neutral and singly ionized state, though only a handful of (one to five) Ti lines can be measured in the Tri II stars. The abundance of Ti I is affected by non-LTE (NLTE) effects (e.g., Mashonkina et al. 2017), so we only plot Ti II abundances in Figure 2 both to avoid NLTE effects and because a Ti II line can be measured in all four of our stars. The literature sample also uses Ti II whenever possible.

4.3. Odd-Z Elements: Na, Al, K, Sc

Sodium is measured from the Na D lines for GruI-032, GruI-038, and TriII-40. While we can identify the presence of Na D lines in TriII-46, the lines are too noisy for a reliable abundance measurement. An upper limit [Na/Fe] < 1.04 is found from the subordinate Na lines near 8190 Å, and for completeness we include the best estimate of equivalent widths for the Na D lines in Table 2. NLTE corrections are not applied since most stars in the literature comparison sample do not have these corrections, but the grid from Lind et al. (2011) gives corrections of −0.28 for GruI-032, −0.32 for GruI-038, and −0.06 for TriII-40. The two Gru I stars have solar ratios of Na, following the usual halo trend. In contrast, TriII-40 has significantly subsolar [Na/Fe] $= -0.79 \pm 0.22$ that is an outlier from the halo trend, as first reported by Venn et al. (2017). A similarly low [Na/Fe] ratio has previously been seen in one of three stars in the UFD Coma Berenices (Frebel et al. 2010b). The primordial (first-generation) population of stars in GCs also have low Na, but all with [Na/Fe] > -0.5 (Gratton et al. 2012).

[9] ftp://ftp.noao.edu/catalogs/arcturusatlas

Aluminum and scandium are only measured in the Gru I stars. Al is determined from a single line at 3961 Å. Given the low S/N in this region, Al is the least certain abundance of all elements measured here. The measurement is consistent with that of other halo stars at [Fe/H] ≈ -2.5, but it is not a meaningful constraint. Sc lines in Gru I are synthesized owing to hyperfine structure (Kurucz & Bell 1995), and the abundances are also similar to other halo stars. For completeness, we place Sc upper limits in the Tri II stars with some weak red lines that provide no interesting constraint.

Potassium has two strong lines at 7665 and 7699 Å. These lines are located near several telluric absorption features. Figure 5 shows these two lines and the best-fit synthetic spectrum or upper limits. The top two spectra are Gru I observations, where observations were conducted within the span of 1 month, so the telluric features do not move much owing to heliocentric corrections. Both Gru I stars have K lines that are easily distinguished from the telluric features. The bottom two spectra of Figure 5 are Tri II observations, which were conducted in 2015 December and 2016 September. The heliocentric correction is different between these epochs by ∼40 km s^{-1}, so the telluric features shift by ≈1 Å between 2015 and 2016. We emphasize this for TriII-40 by showing individual frames from 2015 December (thin blue lines) and 2016 September (thin cyan lines). Note that we used `scombine` in IRAF with `avsigclip` rejection to obtain the co-added black spectra, so it tends to follow the telluric lines from 2016 September (four exposures) rather than 2015 December (two exposures). The λ7699 line is detected in TriII-40. It is significantly blended with a telluric line in the 2015 December observations (see Venn et al. 2017; Figure 4, dark blue lines here) but cleanly separated in the 2016 September observations. We find [K/Fe] $= 0.8$ in TriII-40, in agreement with the measurement by Venn et al. (2017). The λ7665 line is severely blended with telluric lines in both epochs, so we do not use it but just highlight its position in Figure 5 with a synthesized K line. Neither K line is detected for TriII-46, and an upper limit [K/Fe] < 0.77 is set with the λ7699 line. We could not account for the telluric lines when setting this upper limit, but this makes the limit more conservative. NLTE corrections have not been applied, but they can be large (as high as −0.4 dex for the most K-enhanced stars in LTE; Andrievsky et al. 2010).

4.4. Iron-peak Elements: Cr, Mn, Co, Ni, Zn

The Fe-peak abundances were determined with equivalent widths, except for Mn, which is synthesized owing to hyperfine structure (Kurucz & Bell 1995).

In Gru I we can constrain Cr, Mn, Co, and Ni, finding that both stars have essentially identical abundances of these

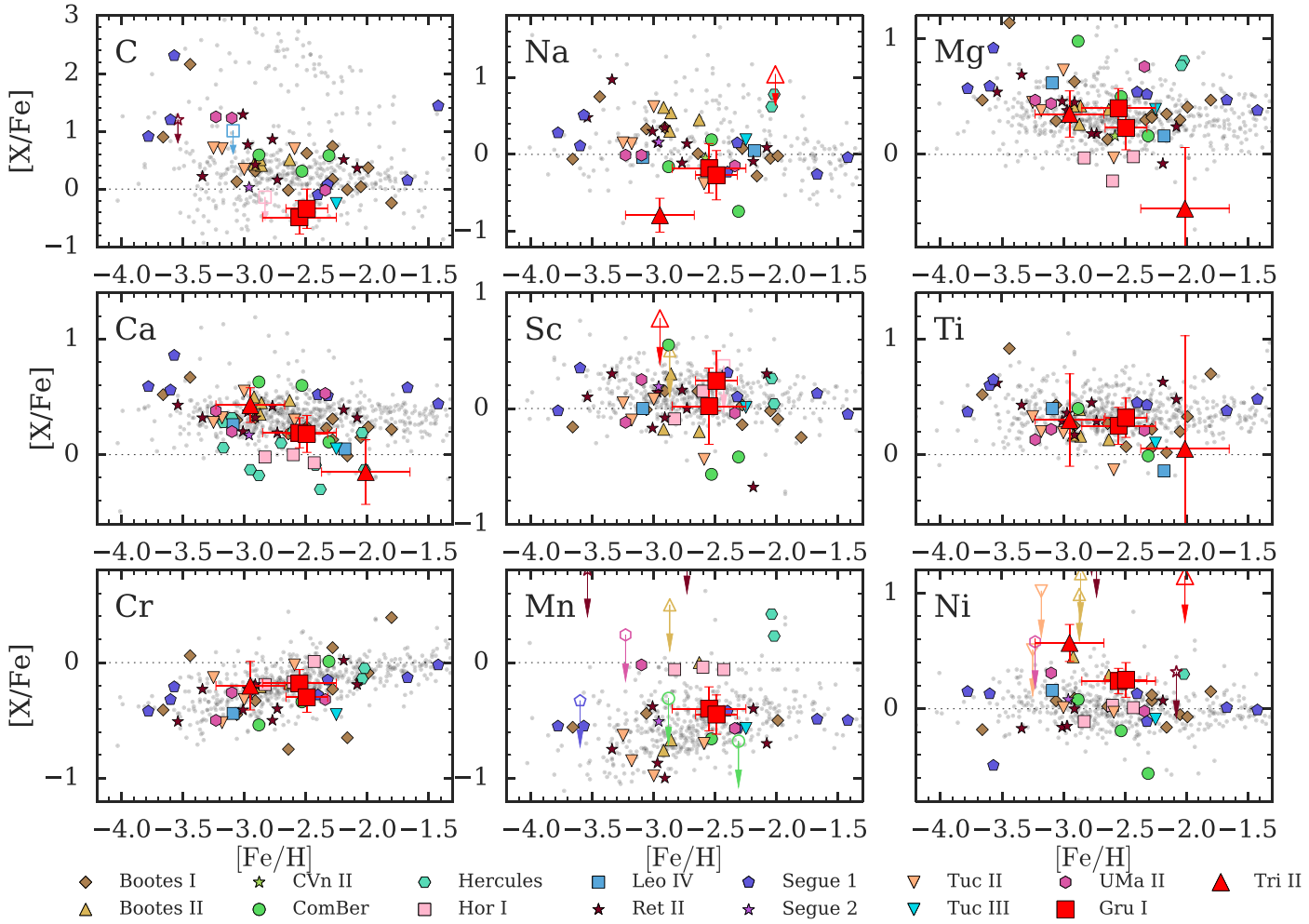

Figure 2. Abundance of light elements in Gru I (red squares) and Tri II (red triangles) compared to halo stars (gray points) and other UFDs (colored points). Upper limits are indicated as open symbols with arrows. The element X is indicated in the upper left corner of each panel. Tri II stars are not plotted for C. Limits on Tri II abundances are above the top axis for Sc and Mn. Essentially all [X/Fe] ratios in these two galaxies follow trends defined by the Milky Way halo stars and other UFDs. The notable exceptions are the Na and Ni in TriII-40 and the low Mg and Ca in TriII-46.

elements. Though the Cr and Mn abundances are similar to those in metal-poor stars in other UFDs or in the Milky Way halo, the Co and Ni abundances are somewhat higher. However, this difference is not very significant, especially for Co, which is derived from only a few bluer lines. One Zn line is marginally detected in GruI-032 with an abundance consistent with the halo trend, though with large uncertainty.

In Tri II, we can detect Cr and Ni in TriII-40 and provide upper limits in TriII-46. Mn, Co, and Zn are unconstrained, as they only have strong lines blueward of 5000 Å. The upper limits for Cr and Ni in TriII-46 are uninteresting. For TriII-40, we detect a normal [Cr/Fe] ratio, but Ni appears significantly enhanced ([Ni/Fe] $= 0.57 \pm 0.16$), in agreement with Kirby et al. (2017) and Venn et al. (2017).

4.5. Neutron-capture Elements: Sr, Ba, Eu

Strontium is detected only in Gru I, as the strong Sr II lines at 4077 and 4215 Å are out of the range of the Tri II (GRACES) spectra. The abundance of both lines is determined with spectrum synthesis. The Sr abundances in these two stars are very similar, [Sr/Fe] ≈ -2, which is much lower than what is found in most halo stars but similar to most UFDs (Figure 4).

Barium is measured with four different lines in the Gru I stars including hyperfine structure and isotope splitting (McWilliam 1998). We use solar isotope ratios (Sneden et al. 2008), but given the low overall abundance, changing this to *r*- or *s*-process ratios does not significantly affect our abundances. GruI-032 has a low [Ba/Fe] ≈ -1.6, but GruI-038 has a much higher Ba abundance [Ba/Fe] ≈ -1.0. This is formally only 1.6σ different, but differential comparison of the line strengths (e.g., the λ6497 line in Figure 1) suggests that the difference is real. We discuss this more in Section 5.1, but both Ba abundances are low and similar to those in most UFDs.

Ba is not detected in either Tri II star, so instead we place 5σ upper limits. The Ba limit for TriII-40 is [Ba/Fe] < -1.25, suggesting a low Ba abundance similar to other UFDs. Kirby et al. (2017) determined [Sr/Fe] $= -1.5$ and [Ba/Fe] $= -2.4$ from their HIRES spectrum of this star, consistent with our upper limit and showing that TriII-40 clearly has very low neutron-capture element abundances. The Ba limit for TriII-46 is only [Ba/Fe] $\lesssim -0.2$, but this is still at the lower envelope of the halo trend (Figure 4).

Eu is not detected in any of these four stars, as expected given the low Sr and Ba abundances. Upper limits are placed

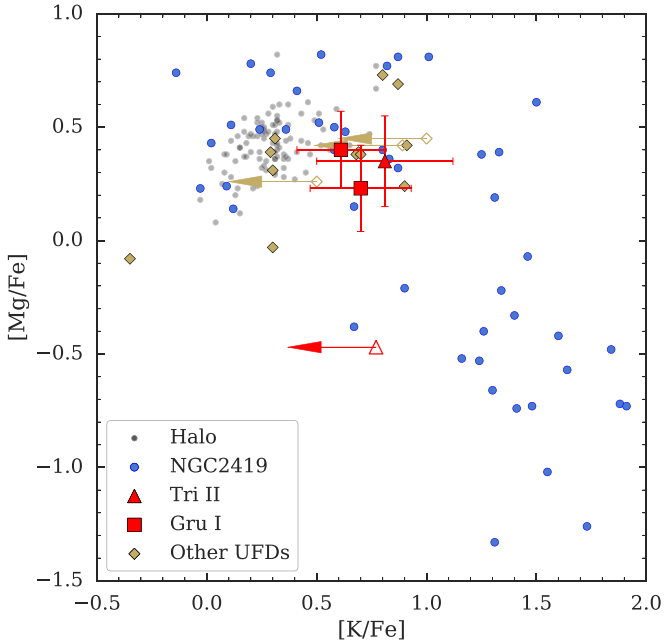

Figure 3. K and Mg abundances of stars in Tri II and Gru I from this work, compared to K and Mg in the stellar halo (Roederer et al. 2014), NGC 2419 (Mucciarelli et al. 2012), and other UFDs (Boo II, Ji et al. 2016d; Ret II, Ji et al. 2016c; Tuc II, Ji et al. 2016b; Segue 2, Roederer & Kirby 2014; Tuc III, Hansen et al. 2017). The K abundance of TriII-46 is not enhanced, so Tri II does not follow the strange K–Mg anticorrelation in NGC 2419. Note that the halo sample here is different than in Figures 2 and 4 because our usual halo compilation does not have K abundances (Frebel 2010). Adapted from Venn et al. (2017).

from the λ4129 line for the Gru I stars (MIKE data) and from the λ6645 line for the Tri II stars (GRACES data).

5. Discussion

5.1. Abundance Anomalies

The abundance ratios of the two stars in Gru I are nearly identical to each other, and similar to typical UFD stars at [Fe/H] ≈ -2.5. The most notable exception is the Ba abundance, where GruI-038 has 0.6 dex higher [Ba/Fe] than GruI-032. After applying corrections from Placco et al. (2014), GruI-038 also has a higher carbon abundance than GruI-032 ([C/Fe] $= +0.57$ vs. $+0.21$, respectively). The differences are both somewhat low significance, and it is reasonable to consider these two stars chemically identical. However, if the differences are real, one possible explanation is that GruI-038 formed from gas that had been polluted by more AGB stars compared to GruI-032. A lower-mass (1–4 $M_{\odot}$) AGB star could add significant Ba and C without changing the Sr abundance too much (e.g., Lugaro et al. 2012). Since AGB winds are low velocity, their C and Ba production would be more inhomogeneously distributed in the star-forming gas of a UFD progenitor (e.g., Emerick et al. 2018). However, many more stars in Gru I would be needed to test this scenario.

We confirm the result from Venn et al. (2017) that TriII-46, the more Fe-rich star in Tri II, has very low [Mg/Fe] and [Ca/Fe] ratios. The standard interpretation is that TriII-46 must have formed after significant enrichment by SNe Ia, and this star does follow the decreasing [α/Fe] trend of other stars in Tri II (Kirby et al. 2017). Indeed, most other UFDs show a similar downturn in [α/Fe] ratios as [Fe/H] increases (Vargas et al. 2013), though Horologium I is unique in that all known stars in the system have low [α/Fe] (Nagasawa et al. 2018), and Segue 1 is unique in that it shows no downturn in α-elements at high [Fe/H] (Frebel et al. 2014). It is actually somewhat surprising that the very low luminosity Tri II appears to have formed stars long enough to be enriched by SNe Ia, since its luminosity is very similar to Segue 1. If Tri II were significantly tidally stripped by now (Kirby et al. 2015a, 2017; Martin et al. 2016b), this would help reconcile enrichment by SNe Ia with the small present-day luminosity. However, the orbital pericenter of Tri II is 20 kpc, where tidal effects are not too strong (Simon 2018), and there are no visible signs of tidal disruption in deep imaging (Carlin et al. 2017). An alternate explanation could be the presence of very prompt SNe Ia (e.g., Mannucci et al. 2006). If this is the case, it may have implications for the single-degenerate versus double-degenerate debate of SN Ia progenitors. Short detonation delay times (~hundreds of Myr) are a common feature of double-degenerate models and less common (though still possible) for single-degenerate models (e.g., Maoz et al. 2014). One way to distinguish these models in Tri II would be to examine Fe-peak elements like Mn, Co, and Ni (see McWilliam et al. 2018), but these elements are unavailable in our GRACES spectra.

Venn et al. (2017) first noticed that the K and Mg abundances in Tri II could match the unusual GC NGC 2419, which displays a K–Mg anticorrelation of unknown origin (Cohen & Kirby 2012; Mucciarelli et al. 2012). If so, then TriII-46 should have very high $1 <$ [K/Fe] < 2 (Figure 3). Our new limit of [K/Fe] $\lesssim 0.8$ in TriII-46 suggests that Tri II probably does not display the same K–Mg anticorrelation as NGC 2419. [K/Fe] is often enhanced in LTE, for both UFD stars and halo stars (Roederer et al. 2014). NLTE effects tend to amplify the strengths of the resonance lines for K-enhanced stars, so they likely contribute to the apparent overabundance of K in these stars (Andrievsky et al. 2010).

We also confirm results from Kirby et al. (2017) and Venn et al. (2017) that TriII-40 has very low [Na/Fe] $= -0.79 \pm 0.22$ and somewhat high [Ni/Fe] $= 0.57 \pm 0.16$. This star has [Fe/H] ~ -3 and enhanced α-elements, so we would nominally expect its abundance ratios to predominantly reflect the yields of metal-poor core-collapse SNe (CCSNe). It is somewhat counter-intuitive to find enhanced Ni and depressed Na in a CCSN, as the production of both elements is positively correlated with the neutron excess in an SN (e.g., Venn et al. 2004; Nomoto et al. 2013). However, this appears to break down at the lowest metallicities, and the online *Starfit* tool[10] finds that a Population III SN progenitor (11.3 $M_{\odot}$, $E = 3 \times 10^{51}$ erg, from the SN yield grid of Heger & Woosley 2010) provides a decent fit to the Mg, Ca, Ti, Fe, and Ni abundances ([Na/Fe] ≈ -1.0, [Ni/Fe] $\approx +0.2$). An alternate possibility is that this [Fe/H] ~ -3 star formed from gas already affected by SNe Ia, as Chandrasekhar-mass explosions can produce high [Ni/Fe] (e.g., Fink et al. 2014) while reducing [Na/Fe] by adding iron. It seems very unlikely to form and explode a white dwarf so early in this galaxy's history, but age and metallicity may be decoupled at early times owing to inhomogeneous metal mixing (e.g., Frebel & Bromm 2012; Leaman 2012; Nomoto et al. 2013). A very prompt population of SNe Ia with merging delay times as low as 30 Myr could also exist (Mannucci et al. 2006). We note that the Na and Ni lines in our spectrum of TriII-46 are very noisy and cannot provide a

[10] http://starfit.org/

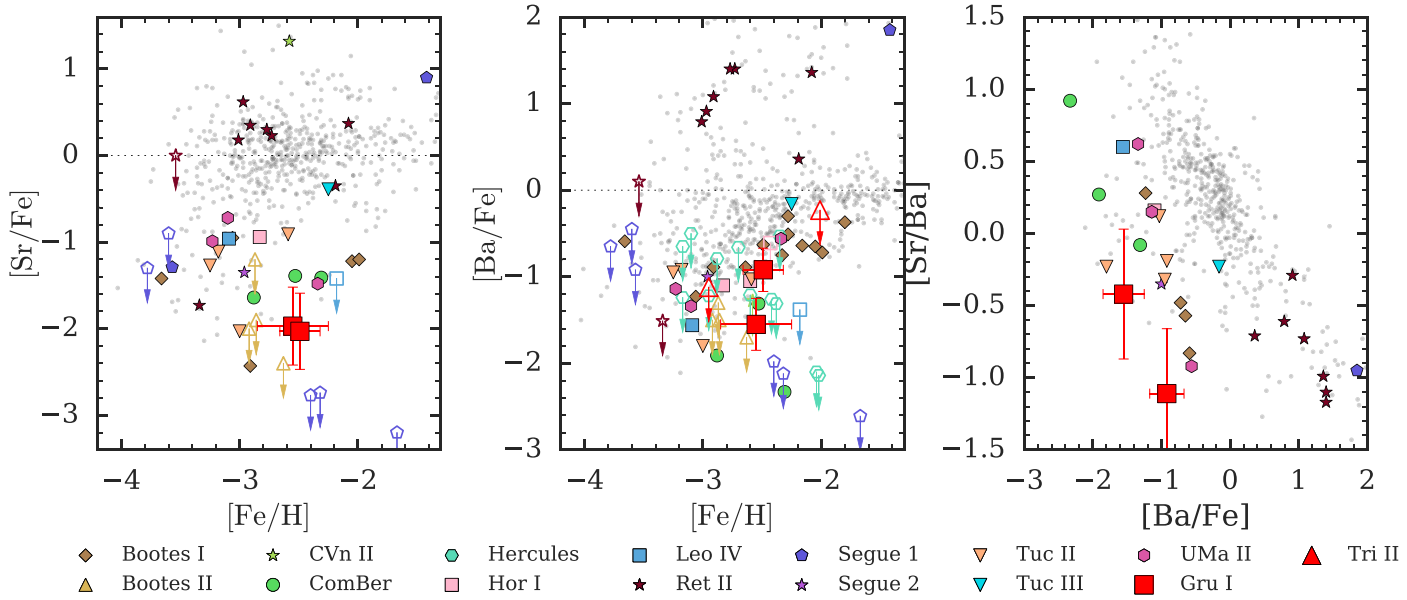

Figure 4. Abundances of Sr and Ba in UFDs compared to halo stars. Symbols are as in Figure 2. The left two panels show the abundance trend with respect to [Fe/H]. Note that there is no constraint on Sr for Tri II stars. The rightmost panel shows that most halo stars cluster near [Sr, Ba/Fe] ≈ 0, but most UFDs are clearly offset to lower Sr and Ba.

reliable abundance, but the best-fit abundance estimates (Table 2) do suggest that this star also has low [Na/Fe] and enhanced [Ni/Fe].

5.2. Classification as Dwarf Galaxy or GC

In this paper, we consider three criteria that can be used to classify Tri II and Gru I as either UFDs or GCs:

(1) a velocity dispersion indicating the presence of dark matter;

(2) an [Fe/H] spread implying the ability to form multiple generations of stars despite SN feedback, or significant internal mixing; and

(3) unusually low neutron-capture element abundances compared to halo stars.

The first two criteria were codified by Willman & Strader (2012) and imply that the stellar system is the result of extended star formation in a dark matter halo. The third criterion is based on previous studies of UFDs confirmed by the other two criteria (e.g., Frebel et al. 2010b, 2014; Simon et al. 2010; Koch et al. 2013; Frebel & Norris 2015), and it has recently been used as a way to distinguish UFD stars from other stars (e.g., Casey & Schlaufman 2017; Kirby et al. 2017; Roederer 2017). Unlike the first two criteria, this is a criterion specifically for the lowest-mass galaxies, rather than defining galaxies in general. Note that violating the criterion also does not preclude an object from being a UFD, as is evident from the *r*-process outliers Ret II and Tuc III that experienced rare *r*-process enrichment events. However, when multiple stars are observed in the same UFD, the majority of stars do tend to have similar neutron-capture element abundances. We discuss possible explanations for criterion 3 in Section 5.3, but first we accept it as an empirical criterion.

5.2.1. Triangulum II

The case of Tri II was already extensively discussed by Kirby et al. (2015a, 2017), Martin et al. (2016b), Venn et al. (2017), and Carlin et al. (2017), generally finding that it is most likely a UFD rather than a star cluster. Our high-resolution abundance results are consistent with the discussion in Venn et al. (2017) and Kirby et al. (2017), namely, that we find a difference in [Fe/H] between these two stars at about 2σ significance, and TriII-46 has lower [α/Fe] ratios compared to TriII-40. Kirby et al. (2017) previously found very low Sr and Ba abundances in TriII-40, and our Ba limit on TriII-46 is consistent with overall low neutron-capture element abundances in Tri II (though additional data are needed to confirm that TriII-46 is well below the halo scatter). Tri II thus likely satisfies criteria 2 and 3, though it is unclear whether it satisfies criterion 1 (see Kirby et al. 2017, Figure 2). Our main additional contribution here is a more stringent upper limit on K in TriII-46 (Figure 3) as discussed above in Section 5.1, which shows that Tri II does not have the abundance signature found in the GC NGC 2419.

5.2.2. Grus I

Walker et al. (2016) identified seven probable members in Gru I. This sample was insufficient to resolve either a velocity dispersion or metallicity dispersion. Our high-resolution follow-up of two stars has found that those stars have indistinguishable [Fe/H]. Thus, Gru I does not currently satisfy criterion 1 or criterion 2 to be considered a galaxy. However, we have found that the neutron-capture element abundances in Gru I are both low and similar to UFDs, satisfying criterion 3. Gru I thus most likely appears to be a UFD, and we expect that further spectroscopic study of Gru I will reveal both metallicity and velocity dispersions. We note that the velocity difference in our two Gru I stars alone does already suggest a potentially significant velocity dispersion.

The mean metallicity determined by Walker et al. (2016) for Gru I is [Fe/H] $\sim -1.4 \pm 0.4$, which placed it far from the luminosity–metallicity trend of other dSph galaxies, while GCs do not have such a relationship. However, the two brightest stars, analyzed here, both have [Fe/H] ~ -2.5, which would be consistent with the mean trend. Only ∼0.3 dex of the difference can be attributed to their metallicity zero-point offset (see Section 3.4). The rest of the discrepancy is due to the fact that Walker et al. (2016) found their other five members of Gru I to

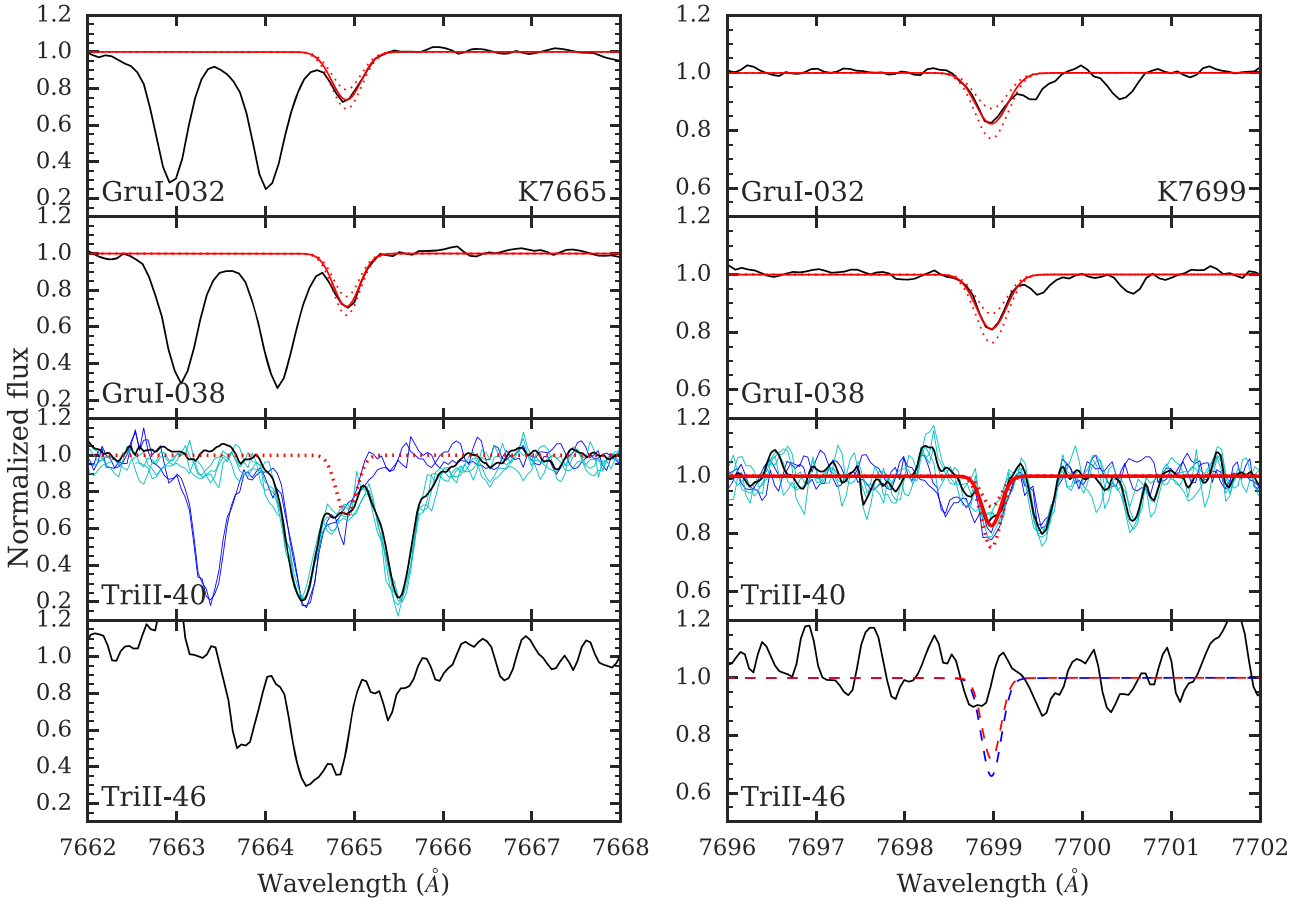

Figure 5. Spectrum around K lines for our four stars. Black lines are the data, solid red lines indicate synthesis fit, and dotted red lines indicate uncertainty. In the third row (TriII-40), dark blue lines indicate data from 2015 December, while cyan lines indicate data from 2016 September, showing how the location of telluric absorption shifts relative to the K line. The λ7699 line is cleanly detected in 2016 September (telluric lines are at 7699.5 and 7701.8 Å). The same abundance is synthesized at the expected strength of the λ7665 line, but we do not use that line because it is too blended with telluric absorption. In the fourth row (TriII-46), the dashed red line is the K upper limit, and the dashed blue line indicates [K/Fe] = 1.

have a much higher [Fe/H] than these two stars, ranging from [Fe/H] $= -2$ to -1. Those five fainter stars are over 1 mag fainter than our stars, currently out of reach for high-resolution spectroscopic abundances, so we cannot test the true metallicity of Gru I with our data. However, those stars also have very low S/N and inferred effective temperatures that are much higher than expected based on photometry alone. We thus suggest that the metallicity of Gru I is probably closer to the value measured from our two stars. Recently, Jerjen et al. (2018) published deep photometry of Gru I, with isochrone-based metallicities of [Fe/H] $= -2.5 \pm 0.3$.

5.3. Why Do Most UFDs Have Low Neutron-capture Element Abundances?

Figure 6 shows the neutron-capture element abundances of UFD stars relative to halo stars and classical dSph stars. Excluding Ret II and Tuc III, it is clear that UFDs have low neutron-capture element abundances relative to these other populations in both Sr and Ba, and most apparent in Sr. The astrophysical origin (or origins) of these low but nonzero neutron-capture element abundances is still an open question (see Section 5.5).

However, the abundance signature of this (or these) low-yield site(s) is usually hidden in more metal-rich stars. This is clearly seen by examining the classical dSph galaxies, which are somewhat more evolved than UFDs owing to their higher mass. In Sculptor, we can see a >1 dex rise in [Sr/Fe] from UFD levels to typical halo star levels occurring at very low metallicity $-4 <$ [Fe/H] < -3.3, while a rise in [Ba/Fe] occurs later, at [Fe/H] ~ -2.5 (see also Jablonka et al. 2015; Mashonkina et al. 2017). Similar trends exist for Sagittarius, Sextans, and Ursa Minor. We highlight Draco and Carina separately, as their stars' [Sr/Fe] ratios stay similarly low to UFDs until [Fe/H] $\gtrsim -2.5$, but unlike UFDs, their [Ba/Fe] ratios rise with [Fe/H]. The UFD Boo I is similar to Draco and Carina and unlike most UFDs in this sense, as well. The rise in Sr and Ba suggests the delayed onset of different, more prolific sources of neutron-capture elements, presumably some combination of AGB stars and neutron star mergers. These higher-yield later-onset sources of Sr and Ba will eventually dominate total Sr and Ba production. Overall, it seems that larger galaxies manage to reach a "normal" halo-like neutron-capture element abundance at lower [Fe/H] than smaller galaxies, implying that they can be enriched by those dominant sources of Sr and Ba (see also Tafelmeyer et al. 2010; Jablonka et al. 2015).

The question of why UFDs have low neutron-capture element abundances thus boils down to why these high-yield sources of neutron-capture elements do not contribute metals to most UFDs while they are forming stars. We can imagine three possible reasons:

1. UFDs do not form enough stars to fully sample all metal yields from a stellar population. If the dominant sources

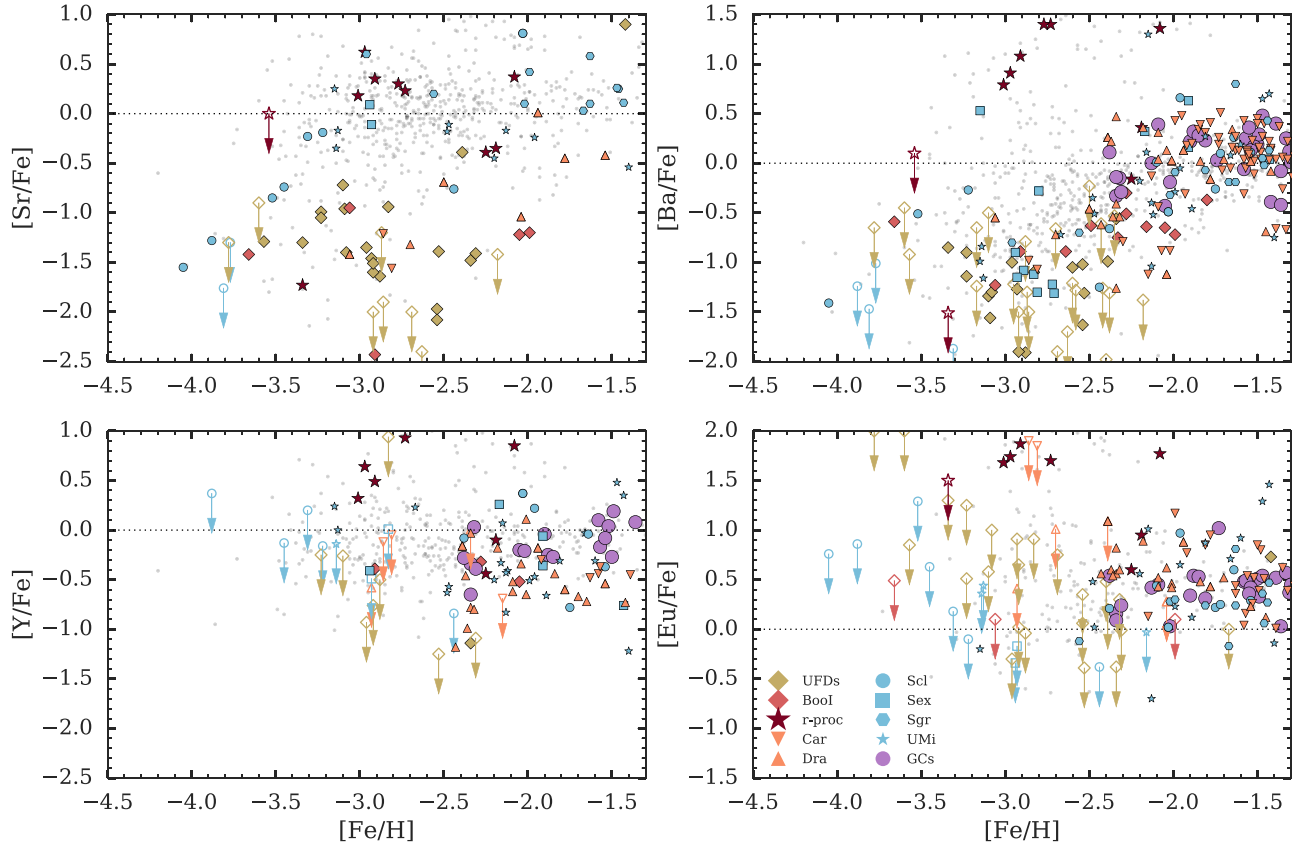

Figure 6. Neutron-capture element abundances for UFDs (yellow diamonds; separating Boo I as red diamonds; and Ret II and Tuc III as large dark-red stars), classical dSphs (blue and orange symbols), GCs (large purple circles), and halo stars (gray points). Classical dSph stars come from Aoki et al. (2009), Cohen & Huang (2009, 2010), Frebel et al. (2010a), Fulbright et al. (2004), Geisler et al. (2005), Hansen et al. (2018), Jablonka et al. (2015), Kirby & Cohen (2012), Norris et al. (2017), Shetrone et al. (2001, 2003), Simon et al. (2015b), Skúladóttir et al. (2015), Tafelmeyer et al. (2010), Tsujimoto et al. (2015, 2017), Ural et al. (2015), and Venn et al. (2012).

of Sr and Ba are produced rarely or stochastically, they will only occasionally enrich a given UFD, so most UFDs would have low [Sr, Ba/Fe] (e.g., Koch et al. 2008, 2013; Simon et al. 2010; Venn et al. 2012, 2017; Ji et al. 2016a).

2. UFDs form in small potential wells, so they do not retain metals very well (e.g., Kirby et al. 2011; Venn et al. 2012). If the dominant sources of Sr and Ba are lost with higher efficiency in UFDs (relative to iron), this would result in low [Sr, Ba/Fe].
3. UFDs form stars for only a short time. If the dominant neutron-capture element sources have long delay times (e.g., neutron star mergers or AGBs), these sources may only produce metals after UFDs have finished forming stars. Then, surviving UFD stars would not preserve the metals from those sources.

We note that Sr and Ba appear to have differing trends, so the explanations for Sr and Ba may differ as well.

As one attempt to distinguish between these possibilities, we consider whether there are correlations with stellar mass or current dynamical mass. Figure 7 shows the absolute magnitude and inferred dynamical mass within the half-light radius for several classical dSphs and UFDs. The yellow points are UFDs that have low [Sr/Fe] and [Ba/Fe]. Blue points are classical dSphs (UMi, Sex, Scl, Sgr) that have regular Sr and Ba trends. In orange we highlight Boo I, Carina, and Draco, which have low Sr at [Fe/H] ~ -3 but Ba behavior similar to the more massive dSphs. We also note that Draco, UMi, and all UFDs have CMDs indicating purely old stellar populations (>10–12 Gyr old), while more luminous dSphs (Carina and above) show evidence for some late-time star formation (Brown et al. 2014; Weisz et al. 2014). There is a broad transition in neutron-capture element content occurring somewhere between $-6 > M_V > -10$ and $10^6 < M_{\rm dyn}/M_\odot < 10^7$, also roughly corresponding to the purely old dSphs. Unfortunately, given the strong correlations between luminosity, dynamical mass, and overall age in this sample, it is hard to distinguish between the three reasons listed above for low neutron-capture elements in UFDs.

Explanation 2 is somewhat disfavored if one accepts two stronger assumptions. First, $M_{\rm dyn}(<r_{1/2})$ is not a good measure of the total halo mass, because the half-light radius is only a tiny fraction of the overall halo size. Correcting for this requires extrapolating an assumed density profile to larger radii, but such extrapolations imply that UFDs and even some of the larger dSphs may all reside in dark halos of similar mass (Strigari et al. 2008). A similar dark halo mass is also expected from a stellar-mass-to-halo-mass relation with large intrinsic scatter (e.g., Jethwa et al. 2018). Second, one must assume that $z = 0$ halo masses are highly correlated with halo masses at the time of star formation. This is true on average in ΛCDM, but it breaks down in specific cases owing to scatter in halo growth histories (e.g., Torrey et al. 2015) and tidal stripping from different subhalo infall times (e.g., Dooley et al. 2014). Together, these two assumptions would imply that neutron-capture element behavior is uncorrelated with halo mass, disfavoring explanation 2. Furthermore, comparison to

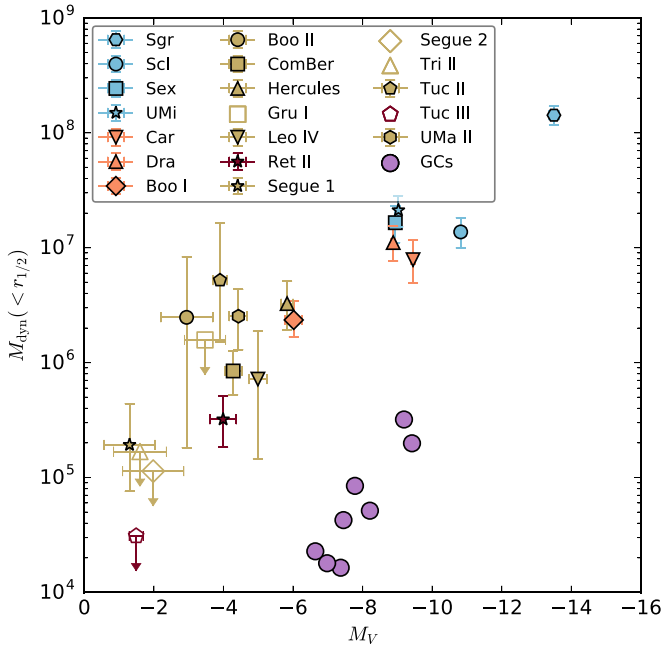

Figure 7. Absolute V magnitude vs. dynamical mass within half-light radius for dSphs with neutron-capture element constraints. Galaxies are color-coded according to their [Sr/Fe] and [Ba/Fe] abundance at $-3.5 \lesssim$ [Fe/H] $\lesssim -2.5$. Yellow points have both low Sr and Ba, orange points have low Sr but regular Ba, and blue points have regular Sr and Ba. For comparison, we also show GCs in the Pritzl et al. (2005) sample with [Fe/H] $\lesssim -2$. The dynamical data and luminosity for dwarf galaxies come from Muñoz et al. (2018), supplemented by Majewski et al. (2003) and Bechtol et al. (2015). Velocity dispersions are from Bellazzini et al. (2008), Kirby et al. (2013a, 2017), Koch et al. (2009), Koposov et al. (2011), Simon & Geha (2007), Simon et al. (2011, 2015a, 2017), J. D. Simon (2019, in preparation), and Walker et al. (2009a, 2009b, 2016). $M_{\rm dyn}$ is computed with the equation in Walker et al. (2009b). GC data are from Harris (2010).

classical dSphs suggests that the short star formation timescale (explanation 3) is unlikely for Sr: more massive dSphs like Scl and Sgr are much more efficient at forming stars, but they are already Sr-enriched at [Fe/H] ~ -3. It may thus be the case that explanation 1 is the most likely one for Sr, i.e., that the dominant source of Sr is stochastically produced. However, explanations 1 and 3 both remain viable for Ba, and explanation 2 remains for both Sr and Ba as well if the two stronger assumptions do not hold.

5.4. Comparison to GCs

GCs have very different neutron-capture element abundances than UFDs. Figure 6 shows the mean abundances of GCs as purple circles (compiled in Pritzl et al. 2005[11]). Sr is usually not measured in GCs, so we also show Y (which has similar nucleosynthetic origins to Sr). It is immediately obvious that all neutron-capture elements in GCs closely trace the overall halo trend, as well as more metal-rich stars in classical dSphs. In contrast, UFDs tend to lie at the extremes of the halo trend.

The origin of GCs is unknown, but one class of theories posits that metal-poor GCs form as the dominant stellar component of a small dark matter halo, rather than as a part of a larger galaxy (e.g., Forbes et al. 2018, and references therein). Such theories usually have GCs form in the *same* dark matter halos as UFDs (i.e., $\sim 10^8\,M_\odot$ dark matter halos that experience atomic line cooling), but something (e.g., a gas-rich merger) triggers them to become GCs instead of UFDs (e.g., Griffen et al. 2010; Trenti et al. 2015; Ricotti et al. 2016; Creasey et al. 2019). However, if GCs do form in these small atomic cooling halos, their neutron-capture element enrichment should match that of UFDs, i.e., be very low, or at least show significant GC-to-GC scatter.[12] The difference in neutron-capture element abundances thus seems to imply that the known metal-poor GCs in the Milky Way do *not* form in their own $\sim 10^{7-8}\,M_\odot$ dark matter halos, but instead trace the chemical evolution of a larger galaxy. This matches the model of Boylan-Kolchin (2017), who finds a minimum mass threshold for GC formation of $\sim 10^9\,M_\odot$ at $z = 6$.

Note that the neutron-capture element abundances are not affected by the multiple abundance populations usually discussed in GCs (e.g., Gratton et al. 2004; Roederer 2011). Those variations in lighter abundances are due to an internal mechanism, rather than tracing the natal abundance of the gas from which the GCs formed (see, e.g., Gratton et al. 2012; Bastian & Lardo 2018, and references therein).

5.5. On the Origin of the Ubiquitous Neutron-capture Element Floor

We briefly discuss the most viable candidates for this ubiquitous low-yield neutron-capture element source occurring at low metallicity. This is important not just for understanding UFD enrichment but also for the most metal-poor halo stars, where Sr and/or Ba appear to be ubiquitously present at the level [Sr, Ba/H] ~ -6 (Roederer 2013).[13] The sources must explain the ubiquitous presence of both Sr and Ba, the overall low but nonzero yield of both Sr and Ba, and the fact that the [Sr/Ba] ratio in UFDs varies over $\sim$2 dex.

Neutrino-driven wind. The high-entropy neutrino-driven wind in CCSNe was initially thought to be a promising site for Sr and Ba production in the r-process (e.g., Woosley & Hoffman 1992), but contemporary simulations suggest wind entropies an order of magnitude too low to produce the full set of r-process elements up to uranium (e.g., Arcones et al. 2007). It still seems that this mechanism robustly produces a limited form of the r-process that always synthesizes Sr, but a little bit of Ba only under extreme conditions (e.g., neutron star mass $>2\,M_\odot$, Wanajo 2013). Supporting this, Mashonkina et al. (2017) recently argued for two types of Sr production, one of which was highly correlated with Mg, implying that CCSNe could produce Sr alone. However, current models suggest that even extreme neutrino-driven winds cannot produce [Sr/Ba] $\sim$ 0 (Arcones & Montes 2011; Wanajo 2013), so while they may

[11] We have removed NGC 5897, NGC 6352, and NGC 6362 from this compilation, which were outliers in [Ba/Fe]. These three GCs were all observed by Gratton (1987) and scaled to a common $\log gf$ scale by Pritzl et al. (2005). However, the abundances derived by Gratton (1987) appear to conflict with the $\log gf$, and we suspect a typographical error for $\log gf$. We confirm this in NGC 5897 with more recent measurements by Koch & McWilliam (2014).

[12] At least one metal-poor GC, M15, does show a significant *internal* dispersion in neutron-capture element abundances (>0.6 dex; Sneden et al. 1997). Some other GCs might also display such a dispersion, though it is much smaller (0.3 dex) and could be due to systematic effects (Cohen 2011; Roederer 2011; Roederer & Thompson 2015). Either way, this dispersion is not enough to match the neutron-capture element deficiency seen in most UFD stars with [Fe/H] $\gtrsim -2.5$.

[13] To our knowledge, the only star with limits below this threshold is a star with no detected Fe, SMSS 0313−6708, with extremely low limits [Sr/H] < -6.7 and [Ba/H] < -6.1 (Keller et al. 2014).

be an important factor, they probably are not the only source of neutron-capture elements in most UFDs.

Magnetorotationally driven jets. A dying massive star with extremely strong magnetic fields and fast rotation speeds can launch a neutron-rich jet that synthesizes copious Sr and Ba in the *r*-process (e.g., Winteler et al. 2012; Nishimura et al. 2015). It is still debated whether such extreme conditions can be physically achieved in massive star evolution (e.g., Rembiasz et al. 2016a, 2016b; Mösta et al. 2017). However, if the conditions are less extreme, such SNe can actually produce both Sr and Ba without synthesizing the heaviest *r*-process elements in a delayed jet (Nishimura et al. 2015, 2017; Mösta et al. 2017). These more moderate rotation speeds and magnetic fields may be more plausible results of massive and metal-poor stellar evolution, and so the rate of these moderate jet explosions could occur much more often than is invoked to explain prolific *r*-process yields. If so, then we propose that delayed magnetorotationally driven jets are a viable source of the low Sr and Ba abundances in UFDs. Additional modeling focusing on the frequency of less extreme jets is needed for a more detailed evaluation, and zinc abundances may help as well (Ji & Frebel 2018).

Spinstars. Spinstars are rapidly rotating massive stars that can produce Sr and Ba in the *s*-process (e.g., Meynet et al. 2006). The amount of rotation changes the amount of internal mixing in the star, allowing these models to produce a wide range of [Sr/Ba] ratios, though the amount of Ba is still subject to nuclear reaction rate uncertainties (Cescutti et al. 2013; Frischknecht et al. 2016; Choplin et al. 2018). The fiducial spinstar models in Frischknecht et al. (2016) underproduce Sr and Ba by a factor of >100 to explain the observed values in UFDs (e.g., Ji et al. 2016b), and having hundreds of spinstars in each UFD is unlikely given that there are only hundreds of massive stars to begin with in each galaxy. However, extreme spinstar models with particularly fast rotation velocities and a modified nuclear reaction rate increase the abundance yields by a factor >10 (Frischknecht et al. 2012, 2016; Cescutti et al. 2013).[14] These models also produce [C/Sr] and [C/Ba] $\sim +2.0$, consistent with or somewhat lower than the C abundances in UFDs like Gru I. The [C/Fe] ratios are very high (>3.0), but the spinstar yields do not include any carbon or iron generated in a SN explosion, which would reduce this extreme abundance ratio. Thus, the extreme spinstar models are also a viable source for the neutron-capture elements found in UFDs.

Note that rotation is not the only way that neutron-capture processes can occur in metal-poor or metal-free stars, as it is just one of many possible mechanisms that can induce internal mixing and thus create free neutrons. Recently, Banerjee et al. (2018) and Clarkson et al. (2018) have shown that proton ingestion into convective He shells can result in a low level of *s*-, *i*-, and *r*-processes even in metal-free stars. Some of the metal-poor models by Banerjee et al. (2018) are able to explain the low but nonzero amounts of Sr and Ba found in UFDs, as well as the diversity of [Sr/Ba] ratios.

An unknown low-yield r-process source. As of now, binary neutron star mergers are the only confirmed source of the full *r*-process (i.e., produces all elements from the first through third *r*-process peaks). However, there is evidence from halo stars with low Sr and Ba that UFDs are enriched by a low-yield (or heavily diluted) version of the same abundance pattern. Roederer (2017) found three halo stars with low Sr and Ba, as well as Eu detections consistent with the *r*-process ($-4 <$ [Eu/H] < -3.5). Casey & Schlaufman (2017) found a halo star with [Sr, Ba/H] ≈ -6, with [Sr/Ba] ~ 0 consistent with the full *r*-process. Assuming that these halo stars originated in now tidally disrupted UFDs, that might imply that a low-yield but robust *r*-process does occur. This has long been assumed to take place in some subset of CCSNe, but as mentioned above, current models cannot achieve this reliably. However, UFDs display variations in [Sr/Ba] that cannot be explained by just a single *r*-process.

Disentangling these different sites will require determining abundances of neutron-capture elements other than Sr and Ba in UFD stars. Given the distance to known UFDs, this will require significant time investments with echelle spectrographs on 30 m class telescopes. In the meantime, progress can be made by study of bright, nearby halo stars with low Sr and Ba abundances (e.g., Roederer 2017). For this purpose, the best stars are the relatively Fe-rich but Sr- and Ba-poor stars, as these are the ones most clearly associated with UFDs (Figure 6). Such stars are expected to compose 1%–3% of halo stars at $-2.5 <$ [Fe/H] < -2.0 (Brauer et al. 2018).

6. Conclusion

We present detailed chemical abundances from high-resolution spectroscopy of two stars in Gru I and two stars in Tri II. Overall, the abundance ratios of these stars are generally similar to those found in other UFDs, including extremely low neutron-capture element abundances. The Gru I stars are nearly chemically identical, except for possibly a different Ba abundance. A possible similarity between Tri II and the cluster NGC 2419 is probably ruled out by a new K upper limit, and there may also be an anomaly in Na and Ni (Section 5.1).

The velocity and metallicity dispersions of Gru I and Tri II have not been decisive about whether they are UFDs or GCs, but we conclude that they are both likely UFDs rather than GCs because both systems have extremely low neutron-capture element abundances (Section 5.2). We thus expect future observations of these systems to confirm metallicity spreads, as well as significant velocity dispersions or signs of tidal disruption.

The low neutron-capture element abundances in UFDs reflect chemical enrichment at the extreme low-mass end of galaxy formation in ΛCDM (Section 5.3): stochastic enrichment, metal loss in winds, and short star formation durations. The dissimilarity in neutron-capture elements also suggests that GCs and UFDs do not form in the same environments, and thus that GCs probably did not form in their own dark matter halos (Section 5.4). However, the nucleosynthetic origin of the low neutron-capture element abundances in UFDs like Gru I and Tri II is still an open question (Section 5.5).

We thank Nidia Morrell for assisting with MIKE observations of Gru I; Kristin Chiboucas and Lison Malo for assistance with GRACES and data reduction; Vini Placco for computing carbon corrections; and Projjwal Banerjee, Gabriele Cescutti, Anirudh Chiti, Brendan Griffen, Evan Kirby, Andrew McWilliam, Tony Piro, and Ása Skúladóttir for useful discussions. A.P.J. is supported by NASA through Hubble Fellowship grant *HST*-HF2-51393.001 awarded by the Space Telescope Science Institute, which is operated by the Association of Universities

[14] Yields from http://www.astro.keele.ac.uk/shyne/datasets/s-process-yields-from-frischknecht-et-al-12-15.

for Research in Astronomy, Inc., for NASA, under contract NAS5-26555. J.D.S. and T.T.H. acknowledge support from the National Science Foundation under grant AST-1714873. A.F. acknowledges support from NSF grants AST-1255160 and AST-1716251. K.A.V. acknowledges funding from the National Science and Engineering Research Council of Canada (NSERC), funding reference no. 327292-2006. Based on observations obtained with ESPaDOnS, located at the Canada–France–Hawaii Telescope (CFHT). CFHT is operated by the National Research Council of Canada, the Institut National des Sciences de l'Univers of the Centre National de la Recherche Scientique of France, and the University of Hawai'i. ESPaDOnS is a collaborative project funded by France (CNRS, MENESR, OMP, LATT), Canada (NSERC), CFHT, and ESA. ESPaDOnS was remotely controlled from the Gemini Observatory, which is operated by the Association of Universities for Research in Astronomy, Inc., under a cooperative agreement with the NSF on behalf of the Gemini partnership: the National Science Foundation (United States), the National Research Council (Canada), CONICYT (Chile), Ministerio de Ciencia, Tecnologa e Innovacin Productiva (Argentina) and Ministrio da Cincia, Tecnologia e Inovao (Brazil). This research has made use of the SIMBAD database, operated at CDS, Strasbourg, France (Wenger et al. 2000), and NASA's Astrophysics Data System Bibliographic Services.

Facilities: Magellan-Clay (MIKE, Bernstein et al. 2003), Gemini-N (GRACES, Chene et al. 2014; Donati 2003)

Software: CarPy (Kelson 2003), OPERA (Martioli et al. 2012), IRAF, MOOG (Sneden 1973; Sobeck et al. 2011), SMH (Casey 2014), `numpy` (van der Walt et al. 2011), `scipy` (Jones et al. 2001), `matplotlib` (Hunter 2007), `pandas` (McKinney 2010), `seaborn`, (Waskom et al. 2016), `astropy` (Astropy Collaboration et al. 2013).

ORCID iDs

Alexander P. Ji https://orcid.org/0000-0002-4863-8842
Anna Frebel https://orcid.org/0000-0002-2139-7145
Kim A. Venn https://orcid.org/0000-0003-4134-2042
Terese T. Hansen https://orcid.org/0000-0001-6154-8983

References

Andrievsky, S. M., Spite, M., Korotin, S. A., et al. 2010, A&A, 509, A88
Aoki, W., Arimoto, N., Sadakane, K., et al. 2009, A&A, 502, 569
Arcones, A., Janka, H.-T., & Scheck, L. 2007, A&A, 467, 1227
Arcones, A., & Montes, F. 2011, ApJ, 731, 5
Asplund, M., Grevesse, N., Sauval, A. J., & Scott, P. 2009, ARA&A, 47, 481
Astropy Collaboration, Robitaille, T. P., Tollerud, E. J., et al. 2013, A&A, 558, A33
Banerjee, P., Qian, Y.-Z., & Heger, A. 2018, ApJ, 865, 120
Bastian, N., & Lardo, C. 2018, ARA&A, 56, 83
Battaglia, G., Irwin, M., Tolstoy, E., et al. 2008, MNRAS, 383, 183
Bechtol, K., Drlica-Wagner, A., Balbinot, E., et al. 2015, ApJ, 807, 50
Bellazzini, M., Ibata, R. A., Chapman, S. C., et al. 2008, AJ, 136, 1147
Belokurov, V., Zucker, D. B., Evans, N. W., et al. 2007, ApJ, 654, 897
Benson, A. J., Frenk, C. S., Lacey, C. G., Baugh, C. M., & Cole, S. 2002, MNRAS, 333, 177
Bernstein, R., Shectman, S. A., Gunnels, S. M., Mochnacki, S., & Athey, A. E. 2003, Proc. SPIE, 4841, 1694
Bland-Hawthorn, J., Sutherland, R., & Webster, D. 2015, ApJ, 807, 154
Boylan-Kolchin, M. 2017, MNRAS, 472, 3120
Brauer, K., Ji, A. P., Frebel, F., et al. 2018, ApJ, submitted (arXiv:1809.05539)
Bromm, V., & Yoshida, N. 2011, ARA&A, 49, 373
Brown, T. M., Tumlinson, J., Geha, M., et al. 2014, ApJ, 796, 91
Bullock, J. S., Kravtsov, A. V., & Weinberg, D. H. 2000, ApJ, 539, 517
Carlin, J. L., Sand, D. J., Muñoz, R. R., et al. 2017, AJ, 154, 267
Casey, A. R. 2014, arXiv:1405.5968
Casey, A. R., & Schlaufman, K. C. 2017, ApJ, 850, 179
Castelli, F., & Kurucz, R. L. 2004, arXiv:astro-ph/0405087
Cescutti, G., Chiappini, C., Hirschi, R., Meynet, G., & Frischknecht, U. 2013, A&A, 553, A51
Chene, A.-N., Padzer, J., Barrick, G., et al. 2014, Proc. SPIE, 9151, 915147
Chiti, A., Frebel, A., Ji, A. P., et al. 2018, ApJ, 857, 74
Choplin, A., Hirschi, R., Meynet, G., et al. 2018, arXiv:1807.06974
Clarkson, O., Herwig, F., & Pignatari, M. 2018, MNRAS, 474, L37
Cohen, J. G. 2011, ApJL, 740, L38
Cohen, J. G., & Huang, W. 2009, ApJ, 701, 1053
Cohen, J. G., & Huang, W. 2010, ApJ, 719, 931
Cohen, J. G., & Kirby, E. N. 2012, ApJ, 760, 86
Creasey, P., Sales, L. V., Peng, E. W., & Sameie, O. 2019, MNRAS, 482, 219
Donati, J.-F. 2003, in ASP Conf. Ser. 307, Solar Polarization, ed. J. Trujillo-Bueno & J. Sanchez Almeida (San Francisco, CA: ASP), 41
Dooley, G. A., Griffen, B. F., Zukin, P., et al. 2014, ApJ, 786, 50
Emerick, A., Bryan, G. L., & Mac Low, M.-M. 2018, arXiv:1807.07182
Feltzing, S., Eriksson, K., Kleyna, J., & Wilkinson, M. I. 2009, A&A, 508, L1
Fink, M., Kromer, M., Seitenzahl, I. R., et al. 2014, MNRAS, 438, 1762
Forbes, D. A., Bastian, N., Gieles, M., et al. 2018, arXiv:1801.05818
François, P., Monaco, L., Bonifacio, P., et al. 2016, A&A, 588, A7
Frebel, A. 2010, AN, 331, 474
Frebel, A., & Bromm, V. 2012, ApJ, 759, 115
Frebel, A., Casey, A. R., Jacobson, H. R., & Yu, Q. 2013, ApJ, 769, 57
Frebel, A., Kirby, E. N., & Simon, J. D. 2010a, Natur, 464, 72
Frebel, A., & Norris, J. E. 2015, ARA&A, 53, 631
Frebel, A., Norris, J. E., Gilmore, G., & Wyse, R. F. G. 2016, ApJ, 826, 110
Frebel, A., Simon, J. D., Geha, M., & Willman, B. 2010b, ApJ, 708, 560
Frebel, A., Simon, J. D., & Kirby, E. N. 2014, ApJ, 786, 74
Frischknecht, U., Hirschi, R., Pignatari, M., et al. 2016, MNRAS, 456, 1803
Frischknecht, U., Hirschi, R., & Thielemann, F.-K. 2012, A&A, 538, L2
Fulbright, J. P., Rich, R. M., & Castro, S. 2004, ApJ, 612, 447
Geisler, D., Smith, V. V., Wallerstein, G., Gonzalez, G., & Charbonnel, C. 2005, AJ, 129, 1428
Gilmore, G., Norris, J. E., Monaco, L., et al. 2013, ApJ, 763, 61
Gratton, R., Sneden, C., & Carretta, E. 2004, ARA&A, 42, 385
Gratton, R. G. 1987, A&A, 179, 181
Gratton, R. G., Carretta, E., & Bragaglia, A. 2012, A&ARv, 20, 50
Griffen, B. F., Drinkwater, M. J., Thomas, P. A., Helly, J. C., & Pimbblet, K. A. 2010, MNRAS, 405, 375
Hansen, C. J., El-Souri, M., Monaco, L., et al. 2018, ApJ, 855, 83
Hansen, T. T., Simon, J. D., Marshall, J. L., et al. 2017, ApJ, 838, 44
Harris, W. E. 2010, arXiv:1012.3224
Heger, A., & Woosley, S. E. 2010, ApJ, 724, 341
Hinkle, K., Wallace, L., Livingston, W., et al. 2003, in Cambridge Workshop on Cool Stars, Stellar Systems, and the Sun 12, The Future of Cool-Star Astrophysics, ed. A. Brown, G. M. Harper, & T. R. Ayres (Boulder, CO: University of Colorado), 851
Hunter, J. D. 2007, CSE, 9, 90
Ishigaki, M. N., Aoki, W., Arimoto, N., & Okamoto, S. 2014, A&A, 562, A146
Jablonka, P., North, P., Mashonkina, L., et al. 2015, A&A, 583, A67
Jerjen, H., Conn, B., Kim, D., & Schirmer, M. 2018, arXiv:1809.02259
Jethwa, P., Erkal, D., & Belokurov, V. 2018, MNRAS, 473, 2060
Ji, A. P., & Frebel, A. 2018, ApJ, 856, 138
Ji, A. P., Frebel, A., Chiti, A., & Simon, J. D. 2016a, Natur, 531, 610
Ji, A. P., Frebel, A., Ezzeddine, R., & Casey, A. R. 2016b, ApJL, 832, L3
Ji, A. P., Frebel, A., Simon, J. D., & Chiti, A. 2016c, ApJ, 830, 93
Ji, A. P., Frebel, A., Simon, J. D., & Geha, M. 2016d, ApJ, 817, 41
Jones, E., Oliphant, T., Peterson, P., et al. 2001, SciPy: Open source scientific tools for Python, http://www.scipy.org/
Keller, S. C., Bessell, M. S., Frebel, A., et al. 2014, Natur, 506, 463
Kelson, D. D. 2003, PASP, 115, 688
Kim, Y.-C., Demarque, P., Yi, S. K., & Alexander, D. R. 2002, ApJS, 143, 499
Kirby, E. N., Boylan-Kolchin, M., Cohen, J. G., et al. 2013a, ApJ, 770, 16
Kirby, E. N., & Cohen, J. G. 2012, AJ, 144, 168
Kirby, E. N., Cohen, J. G., Guhathakurta, P., et al. 2013b, ApJ, 779, 102
Kirby, E. N., Cohen, J. G., Simon, J. D., et al. 2017, ApJ, 838, 83
Kirby, E. N., Cohen, J. G., Simon, J. D., & Guhathakurta, P. 2015a, ApJL, 814, L7
Kirby, E. N., Guhathakurta, P., Bolte, M., Sneden, C., & Geha, M. C. 2009, ApJ, 705, 328
Kirby, E. N., Martin, C. L., & Finlator, K. 2011, ApJL, 742, L25
Kirby, E. N., Simon, J. D., & Cohen, J. G. 2015b, ApJ, 810, 56
Kirby, E. N., Simon, J. D., Geha, M., Guhathakurta, P., & Frebel, A. 2008, ApJL, 685, L43

Koch, A., Feltzing, S., Adén, D., & Matteucci, F. 2013, A&A, 554, A5
Koch, A., & McWilliam, A. 2014, A&A, 565, A23
Koch, A., McWilliam, A., Grebel, E. K., Zucker, D. B., & Belokurov, V. 2008, ApJL, 688, L13
Koch, A., Wilkinson, M. I., Kleyna, J. T., et al. 2009, ApJ, 690, 453
Koposov, S. E., Belokurov, V., Torrealba, G., & Evans, N. W. 2015a, ApJ, 805, 130
Koposov, S. E., Casey, A. R., Belokurov, V., et al. 2015b, ApJ, 811, 62
Koposov, S. E., Gilmore, G., Walker, M. G., et al. 2011, ApJ, 736, 146
Kurucz, R., & Bell, B. 1995, Atomic Line Data Kurucz CD-ROM No. 23 (Cambridge, MA: Smithsonian Astrophysical Observatory), 23
Kurucz, R. L. 2011, CaJPh, 89, 417
Laevens, B. P. M., Martin, N. F., Ibata, R. A., et al. 2015, ApJL, 802, L18
Leaman, R. 2012, AJ, 144, 183
Lee, D. M., Johnston, K. V., Tumlinson, J., Sen, B., & Simon, J. D. 2013, ApJ, 774, 103
Lee, Y. S., Beers, T. C., Sivarani, T., et al. 2008, AJ, 136, 2022
Lind, K., Asplund, M., Barklem, P. S., & Belyaev, A. K. 2011, A&A, 528, A103
Lugaro, M., Karakas, A. I., Stancliffe, R. J., & Rijs, C. 2012, ApJ, 747, 2
Majewski, S. R., Skrutskie, M. F., Weinberg, M. D., & Ostheimer, J. C. 2003, ApJ, 599, 1082
Mannucci, F., Della Valle, M., & Panagia, N. 2006, MNRAS, 370, 773
Maoz, D., Mannucci, F., & Nelemans, G. 2014, ARA&A, 52, 107
Martin, N. F., Geha, M., Ibata, R. A., et al. 2016a, MNRAS, 458, L59
Martin, N. F., Ibata, R. A., Collins, M. L. M., et al. 2016b, ApJ, 818, 40
Martioli, E., Teeple, D., Manset, N., et al. 2012, Proc. SPIE, 8451, 84512B
Mashonkina, L., Jablonka, P., Pakhomov, Y., Sitnova, T., & North, P. 2017, A&A, 604, A129
Masseron, T., Plez, B., Van Eck, S., et al. 2014, A&A, 571, A47
McConnachie, A. W., & Côté, P. 2010, ApJL, 722, L209
McKinney, W. 2010, in Proc. 9th Python in Science Conf., 51, http://conference.scipy.org/proceedings/scipy2010/mckinney.html
McWilliam, A. 1998, AJ, 115, 1640
McWilliam, A., Piro, A. L., Badenes, C., & Bravo, E. 2018, ApJ, 857, 97
McWilliam, A., Preston, G. W., Sneden, C., & Searle, L. 1995, AJ, 109, 2757
Meynet, G., Ekström, S., & Maeder, A. 2006, A&A, 447, 623
Mösta, P., Roberts, L. F., Halevi, G., et al. 2017, arXiv:1712.09370
Mucciarelli, A., Bellazzini, M., Ibata, R., et al. 2012, MNRAS, 426, 2889
Muñoz, R. R., Côté, P., Santana, F. A., et al. 2018, ApJ, 860, 66
Nagasawa, D. Q., Marshall, J. L., Li, T. S., et al. 2018, ApJ, 852, 99
Nishimura, N., Sawai, H., Takiwaki, T., Yamada, S., & Thielemann, F.-K. 2017, ApJL, 836, L21
Nishimura, N., Takiwaki, T., & Thielemann, F.-K. 2015, ApJ, 810, 109
Nomoto, K., Kobayashi, C., & Tominaga, N. 2013, ARA&A, 51, 457
Norris, J. E., Wyse, R. F. G., Gilmore, G., et al. 2010, ApJ, 723, 1632
Norris, J. E., Yong, D., Venn, K. A., et al. 2017, ApJS, 230, 28
Placco, V. M., Frebel, A., Beers, T. C., & Stancliffe, R. J. 2014, ApJ, 797, 21
Pritzl, B. J., Venn, K. A., & Irwin, M. 2005, AJ, 130, 2140
Rembiasz, T., Guilet, J., Obergaulinger, M., et al. 2016a, MNRAS, 460, 3316
Rembiasz, T., Obergaulinger, M., Cerdá-Durán, P., Müller, E., & Aloy, M. A. 2016b, MNRAS, 456, 3782
Ricotti, M., Parry, O. H., & Gnedin, N. Y. 2016, ApJ, 831, 204
Roederer, I. U. 2011, ApJL, 732, L17
Roederer, I. U. 2013, AJ, 145, 26
Roederer, I. U. 2017, ApJ, 835, 23
Roederer, I. U., & Kirby, E. N. 2014, MNRAS, 440, 2665
Roederer, I. U., Mateo, M., Bailey, J. I., III, et al. 2016, AJ, 151, 82
Roederer, I. U., Preston, G. W., Thompson, I. B., et al. 2014, AJ, 147, 136
Roederer, I. U., Sneden, C., Thompson, I. B., Preston, G. W., & Shectman, S. A. 2010, ApJ, 711, 573
Roederer, I. U., & Thompson, I. B. 2015, MNRAS, 449, 3889
Shetrone, M., Venn, K. A., Tolstoy, E., et al. 2003, AJ, 125, 684
Shetrone, M. D., Côté, P., & Sargent, W. L. W. 2001, ApJ, 548, 592
Simon, J. D. 2018, ApJ, 863, 89
Simon, J. D., Drlica-Wagner, A., Li, T. S., et al. 2015a, ApJ, 808, 95
Simon, J. D., Frebel, A., McWilliam, A., Kirby, E. N., & Thompson, I. B. 2010, ApJ, 716, 446
Simon, J. D., & Geha, M. 2007, ApJ, 670, 313
Simon, J. D., Geha, M., Minor, Q. E., et al. 2011, ApJ, 733, 46
Simon, J. D., Jacobson, H. R., Frebel, A., et al. 2015b, ApJ, 802, 93
Simon, J. D., Li, T. S., Drlica-Wagner, A., et al. 2017, ApJ, 838, 11
Skúladóttir, Á., Tolstoy, E., Salvadori, S., et al. 2015, A&A, 574, A129
Sneden, C., Cowan, J. J., & Gallino, R. 2008, ARA&A, 46, 241
Sneden, C., Kraft, R. P., Shetrone, M. D., et al. 1997, AJ, 114, 1964
Sneden, C. A. 1973, PhD thesis, The Univ. Texas
Sobeck, J. S., Kraft, R. P., Sneden, C., et al. 2011, AJ, 141, 175
Strigari, L. E., Bullock, J. S., Kaplinghat, M., et al. 2008, Natur, 454, 1096
Tafelmeyer, M., Jablonka, P., Hill, V., et al. 2010, A&A, 524, A58
Torrey, P., Wellons, S., Machado, F., et al. 2015, MNRAS, 454, 2770
Trenti, M., Padoan, P., & Jimenez, R. 2015, ApJL, 808, L35
Tsujimoto, T., Ishigaki, M. N., Shigeyama, T., & Aoki, W. 2015, PASJ, 67, L3
Tsujimoto, T., Matsuno, T., Aoki, W., Ishigaki, M. N., & Shigeyama, T. 2017, ApJL, 850, L12
Ural, U., Cescutti, G., Koch, A., et al. 2015, MNRAS, 449, 761
van der Walt, S., Colbert, S. C., & Varoquaux, G. 2011, CSE, 13, 22
Vargas, L. C., Geha, M., Kirby, E. N., & Simon, J. D. 2013, ApJ, 767, 134
Venn, K. A., Irwin, M., Shetrone, M. D., et al. 2004, AJ, 128, 1177
Venn, K. A., Shetrone, M. D., Irwin, M. J., et al. 2012, ApJ, 751, 102
Venn, K. A., Starkenburg, E., Malo, L., Martin, N., & Laevens, B. P. M. 2017, MNRAS, 466, 3741
Walker, M. G., Mateo, M., & Olszewski, E. W. 2009a, AJ, 137, 3100
Walker, M. G., Mateo, M., Olszewski, E. W., et al. 2009b, ApJ, 704, 1274
Walker, M. G., Mateo, M., Olszewski, E. W., et al. 2016, ApJ, 819, 53
Wanajo, S. 2013, ApJL, 770, L22
Waskom, M., Botvinnik, O., O'Kane, D., et al. 2016, seaborn, v0.7.0, Zenodo, doi:10.5281/zenodo.45133
Weisz, D. R., Dolphin, A. E., Skillman, E. D., et al. 2014, ApJ, 789, 147
Wenger, M., Ochsenbein, F., Egret, D., et al. 2000, A&AS, 143, 9
Willman, B., Blanton, M. R., West, A. A., et al. 2005, AJ, 129, 2692
Willman, B., & Strader, J. 2012, AJ, 144, 76
Winteler, C., Käppeli, R., Perego, A., et al. 2012, ApJL, 750, L22
Woosley, S. E., & Hoffman, R. D. 1992, ApJ, 395, 202